CELL BIOLOGY

Sequential CRISPR screening reveals partial NatB inhibition as a strategy to mitigate alpha-synuclein levels in human neurons

Saranya Santhosh Kumar[1,2], Nima N. Naseri[2,3], Sarshan R. Pather[2,4], Erinc Hallacli[5], Alain Ndayisaba[5], Chris Buenaventura[2], Karen Acosta[3], Jennifer Roof[6], Hossein Fazelinia[6,7], Lynn A. Spruce[6], Kelvin Luk[8], Vikram Khurana[5,9,10], Elizabeth Rhoades[3], Ophir Shalem[2,4]*

Alpha-synuclein (αSyn) protein levels correlate with the risk and severity of Parkinson's disease and related neurodegenerative diseases. Lowering αSyn is being actively investigated as a therapeutic modality. Here, we systematically map the regulatory network that controls endogenous αSyn using sequential CRISPR-knockout and -interference screens in an αSyn gene (*SNCA*)–tagged cell line and induced pluripotent stem cell–derived neurons (iNeurons). We uncover αSyn modifiers at multiple regulatory layers, with amino-terminal acetyltransferase B (NatB) enzymes being the most potent endogenous αSyn modifiers in both cell lines. Amino-terminal acetylation protects the cytosolic αSyn from rapid degradation by the proteasome in a Ube2w-dependent manner. Moreover, we show that pharmacological inhibition of methionyl-aminopeptidase 2, a regulator of NatB complex formation, attenuates endogenous αSyn in iNeurons carrying *SNCA* triplication. Together, our study reveals several gene networks that control endogenous αSyn, identifies mechanisms mediating the degradation of nonacetylated αSyn, and illustrates potential therapeutic pathways for decreasing αSyn levels in synucleinopathies.

INTRODUCTION

Alpha-synuclein (αSyn) is a central player in the pathogenesis of Parkinson's disease (PD) and numerous other less-prevalent synucleinopathies. αSyn gene (*SNCA*) mutations and copy number variations cause early-onset familial PD (*1*–*3*). In addition, genetic variations identified in the noncoding regions of *SNCA* are associated with increased αSyn transcription in sporadic PD populations (*4*, *5*), establishing a strong link between elevated αSyn levels and PD pathogenesis. Reducing αSyn levels in preclinical PD models has proven to be beneficial (*6*), motivating multiple ongoing drug development programs to target αSyn production and/or clearance (*7*, *8*). Despite decades of research, little is known about the molecular mechanisms controlling endogenous αSyn (endo-αSyn) levels.

αSyn is primarily a neuronal protein (*9*, *10*), thereby substantially limiting the availability of human cell lines that can be used to study its physiological regulation. Previous genetic screens for αSyn modifiers used exogenous fusion reporters (*11*, *12*) or αSyn-induced toxicity as a phenotypic readout (*13*). A subsequent study identified regulators that affect *SNCA* endogenous mRNA levels as a proxy for protein expression (*14*); however, it remains unclear whether the identified gene modifiers can lead to a sustained reduction of αSyn protein (*15*). Hence, we developed a pipeline to specifically map the regulatory networks controlling endo-αSyn protein levels using pooled CRISPR-based platforms.

To study αSyn in an endogenous and a scalable manner, we first identified a melanoma cell line that naturally expresses αSyn above threshold limits, tagged the endogenous *SNCA* locus, and performed a fluorescent activated cell sorting (FACS)–based genome-wide CRISPR loss of function screen. The screen revealed multiple layers of αSyn protein regulation, including genes associated with 3′-end processing, protein degradation, transcription, and signaling proteins, many of which have been previously associated with PD. We also performed a series of targeted screens in *SNCA*-tagged melanoma cell lines [CRISPR knockout (CRISPR-KO)] and induced pluripotent stem cell (iPSC)–derived neurons [CRISPR interference (CRISPRi)] to enhance the specificity of our primary screen results. The results from both screens highlight numerous common therapeutic modalities, with a special emphasis on the role of N-terminal acetylation (NTA) in maintaining endo-αSyn protein levels. We further explored the subcellular distribution and degradation of αSyn in the absence of NAA25, the enzyme responsible for NTA, and by overexpressing nonacetylated forms of αSyn in multiple cell lines. We also demonstrated that inhibiting methionyl aminopeptidase 2 (METAP2), a negative αSyn modifier identified in our screen, with a small-molecule inhibitor attenuates αSyn levels in iPSC-derived neurons carrying *SNCA* triplication. Collectively, we present large-scale pooled CRISPR-based screens in conjunction with FACS-based readouts to probe the regulatory networks of a disease protein in its native context in two different cell lines. Our study reveals several positive and negative modifiers of αSyn, mechanisms underlying the degradation of nonacetylated αSyn, and effective strategies to lower αSyn in PD patient–derived neurons.

RESULTS

Tagging of *SNCA* gene allows accurate measurement of endo-αSyn protein levels using FACS in mammalian cells

To enable a FACS-based genome-scale screen to reveal modulators of the endogenous protein, we sought to identify cell lines

[1]Department of Bioengineering, School of Engineering and Applied Sciences, University of Pennsylvania, Philadelphia, PA, USA. [2]Center for Cellular and Molecular Therapeutics, Children's Hospital of Philadelphia, Philadelphia, PA, USA. [3]Department of Chemistry, University of Pennsylvania, Philadelphia, PA, USA. [4]Department of Genetics, Perelman School of Medicine, University of Pennsylvania, Philadelphia, PA, USA. [5]Division of Movement Disorders and Ann Romney Center for Neurologic Diseases, Department of Neurology, Brigham and Women's Hospital and Harvard Medical School, Boston, MA, USA. [6]Proteomics Core Facility, The Children's Hospital of Philadelphia, Philadelphia, PA, USA. [7]Department of Biomedical and Health Informatics, The Children's Hospital of Philadelphia, Philadelphia, PA, USA. [8]Department of Pathology and Laboratory Medicine, University of Pennsylvania, Philadelphia, PA, USA. [9]Broad Institute of Harvard and MIT, Cambridge, MA, USA. [10]Harvard Stem Cell Institute, Cambridge, MA, USA.
*Corresponding author. Email: shalemo@upenn.edu

that have been used in the past for CRISPR-KO screening (*16*, *17*) and naturally express αSyn at high levels. We ranked cell lines using publicly available RNA-sequencing data (*18*) based on *SNCA* gene expression (fig. S1A) and confirmed protein expression for some of these cell lines (fig. S1B). We identified several melanoma cell lines derived from the skin epithelium naturally expressed high αSyn (*19*), thus making them compatible with a FACS-based readout. We selected and engineered the SKMEL30 cell line to stably express Cas9, the first 10 β strands of mNeongreen2 ($mNG2_{1–10}$) (*20*), and a tdTomato fluorescent protein using lentiviral integration. tdTomato expression allowed us to control for extrinsic factors that affect protein expression, such as cell size and growth. To accurately measure αSyn in SKMEL30 cells by flow cytometry, we tagged the endo-αSyn by electroporating the preassembled Cas9-ribonucleoprotein (RNP) complex along with a single-stranded DNA repair template to fuse the $mNG2_{11}$ fragment to the C terminus of the *SNCA* gene (Fig. 1A). Edited cell populations were analyzed (fig. S1, C and D) and sorted using flow cytometry. The robust expression levels and localization patterns of αSyn in the isolated clonal population, $SKMEL30^{SNCA\text{-}mNG2}$, were confirmed using microscopy and flow cytometry (Fig. 1, B and C). Next, we performed a genome-wide CRISPR-KO screen (*21*, *22*) by transducing *SNCA*-tagged cells with the lentiviral single-guide RNA (sgRNA) Brunello library (*23*), followed by sorting the cells expressing the top and bottom 20% of the mNG2 levels (endo-αSyn) relative to the control protein (tdTomato expression) (Fig. 1D). We measured the sgRNA abundance in the sorted cell population using next-generation sequencing (NGS).

Genome-wide CRISPR screen identifies the endogenous network controlling αSyn protein levels at multiple regulatory layers

We used the data from sgRNA amplicon sequencing present in the high- and low-expression bins to produce two values per gene: (i) phenotype, which estimates the phenotypic effect by considering the best-performing top two sgRNAs per gene; and (ii) a *P* value that calculates the significance of each gene using all the sgRNAs (*24*). As expected, and as a technical positive control, we found that *SNCA* was the top ranked gene for reducing αSyn protein levels (Fig. 1E). We observed that most of our gene hits were negative modifiers of αSyn rather than positive modifiers, which is expected given the resources a cell would invest in producing versus repressing a given protein (Fig. 1, E and F, and table S1). To test the reproducibility of our screen and exclude gene hits affecting our control (tdTomato), we constructed a secondary sgRNA library consisting of the top gene hits [false discovery rate (FDR) < 0.05], nontargeting controls (NTCs), and essential genes. We then performed two secondary screens at higher cell coverage using either tdTomato as the control protein or cell autofluorescence as an alternative denominator for the fluorescence ratio. We found a high correlation between the phenotypes from the two secondary screens (Fig. 1G and table S2), which validated the regulation of endo-αSyn at multiple layers (fig. S1G). We indeed found a small group of gene knockouts that affected non-αSyn factors (i.e., cell division, growth, and tdTomato expression). These genes were curated and removed from the downstream analysis (Fig. 1G and fig. S1, E and F). We also individually validated top gene hits in an arrayed format and measured the expected change in αSyn protein levels using flow cytometry (Fig. 1H and fig. S1H).

Secondary CRISPRi pooled screen in iNeurons with endogenously tagged *SNCA* identifies gene hits that affect neuronal αSyn levels

To evaluate the effectiveness of the gene hits identified in our preliminary $SKMEL30^{SNCA\text{-}mNG2}$ screens in a neuronal model, we conducted a secondary FACS-based screen in neurons derived from iPSCs (iNeurons). Once again, to better model and measure the abundance of αSyn in iNeurons, we inserted an enhanced green fluorescent protein (eGFP) tag at the C terminus of the transcriptionally silent *SNCA* gene in an already established CRISPRi-iPSC platform (*25*). αSyn is a neuronal protein expressed only following neuronal differentiation. Hence, inserting a fluorescent tag at the endogenous *SNCA* locus requires two-step engineering: insertion of a selectable, expressed marker along with an inactive eGFP and excision of that marker to bring downstream eGFP in frame with *SNCA* (*26*) (Fig. 2A). Following homology-directed repair (HDR)–based editing, we isolated and validated clonal iPSC lines for the intended gene-tagging outcome, differential potential, and genomic stability using junctional polymerase chain reaction (PCR) (fig. S2A), immunofluorescence (fig. S2C), and karyotyping (fig. S2D). We further analyzed the eGFP expression as a proxy for αSyn levels in the validated clone upon neuronal differentiation using microscopy (Fig. 2B), flow cytometry (Fig. 2C), and Western blotting (fig. S2B).

Next, we constructed a focused CRISPRi library consisting of 10 sgRNAs for the gene hits that passed a 5% FDR cutoff in our primary SKMEL30 screen. The targeted library contained approximately 4500 sgRNAs, including 1000 nontargeting sgRNAs, and the spacer sequences for the genes were selected from an existing library (*27*). We transduced *SNCA*-tagged CRISPRi-iPSCs constitutively expressing dead Cas9 fused to transcriptional repression Krüppel associated box domain (dCAS9-KRAB) and Neurogenin2 (Ngn2) with the lentiviral sgRNA library to achieve protein knockdown (KD) of the candidate modifier genes. After 10 days in culture, neuronal differentiation was initiated by adding doxycycline to induce Ngn2 expression. We harvested the iNeurons on days 14 and 28 and used flow cytometry to sort neurons expressing high and low αSyn at 50× cell coverage after sorting (Fig. 2D). sgRNA abundance in each population was measured using NGS.

We normalized the raw sgRNA counts using loess scaling based only on the NTCs to capture changes in the total distribution of sgRNA scores, as it is expected for a large fraction of the sgRNAs to have a phenotypic effect in secondary screens. Consistent with our SKMEL30 screen results, our CRISPRi neuronal screen recovered more αSyn-negative modifier genes than positive modifiers (Fig. 2E and fig. S2E). Comparing results from both time points, we observed a strong correlation in the KD phenotypes between our gene hits and a minor fraction of negative regulators were better captured during the later time point (Fig. 2F and table S3). We further validated the phenotypic effect of knocking down top gene hits that down-regulated αSyn in an arrayed format by transducing *SNCA*-tagged CRISPRi-iPSCs with individual sgRNAs, followed by neuronal differentiation and measurement of αSyn levels using flow cytometry (Fig. 2G and fig. S2F).

Cell line and neuronal screen uncover repressors of αSyn levels

We next examined gene perturbations that resulted in increased αSyn levels. Unlike hits on the lower αSyn arm of the screen, here, we observed smaller effect sizes and lower correlation between the modifiers from the two cell models (fig. S3A).

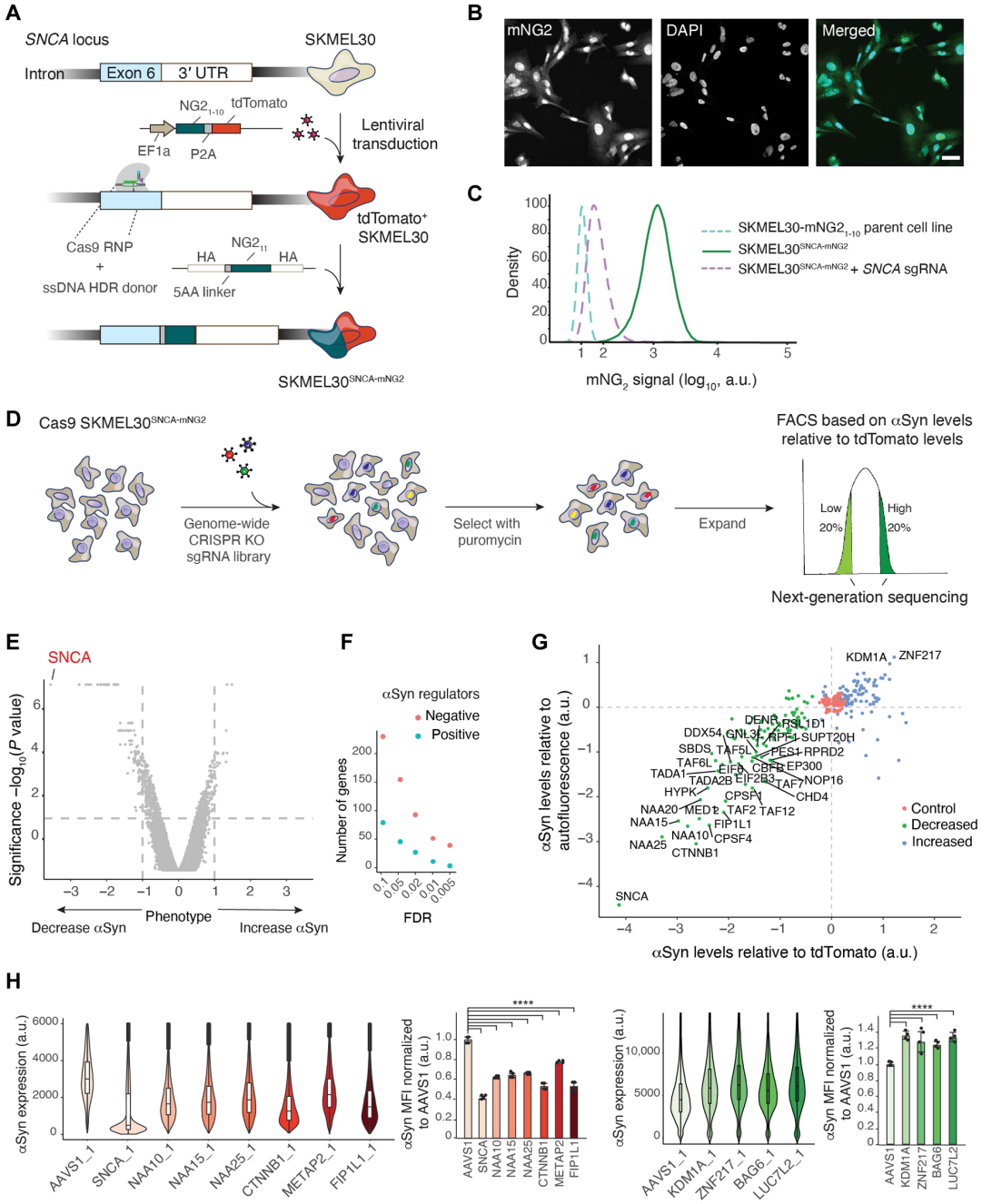

Fig. 1. Genome-wide CRISPR-KO screen in *SNCA*-tagged SKMEL30 cells identifies endo-αSyn regulators. (**A**) Schematic representation of the HDR-based tagging of the gene, *SNCA*, with the split fluorescent protein mNeongreen2 (mNG2) in the SKMEL30 cell line. HA, Homology Arms. The *SNCA*-tagged SKMEL30 clone was termed "SKMEL30$^{SNCA\text{-}mNG2}$." 3′UTR, 3′ untranslated region. (**B**) The validated bi-allelic *SNCA*-tagged clone was analyzed using confocal microscopy for mNG2 expression. Scale bar, 10 μm. (**C**) Histogram plots showing the distribution of mNG2 fluorescence measured using flow cytometry for the untagged, tagged SKMEL30$^{SNCA\text{-}mNG2}$, and SKMEL30$^{SNCA\text{-}mNG2}$ cell line transduced with CRISPR KO guide targeting *SNCA*. a.u., arbitrary units. (**D**) Schematic representation of primary genome-wide screen performed in Cas9 expressing SKMEL30$^{SNCA\text{-}mNG2}$ cells for regulators of αSyn. (**E**) Volcano plot displaying statistical significance on the *y* axis and phenotype on the *x* axis for genes targeted in the αSyn screen. (**F**) Number of significant positive and negative regulators of αSyn identified at different FDR thresholds in the primary screen. (**G**) Comparison of secondary screen results performed using two different controls. Colors represent the effect of the gene knockouts targeted in the secondary screen on αSyn levels. Green: Genes that decrease αSyn levels when knocked out; blue: genes that increase αSyn levels when knocked out; red: control genes. (**H**) Flow cytometry–based quantification of αSyn levels in single-gene KO SKMEL30$^{SNCA\text{-}mNG2}$ cells. Violin plots represent the intensity distribution of mNG2 fluorescence denoting αSyn expression in SKMEL30$^{SNCA\text{-}mNG2}$ cells transduced with CRISPR KO sgRNAs targeting *AAVS1* (NTC), *SNCA* (positive control), and several αSyn negative (red) and positive (green) modulators identified in the screen. Box plot represents interquartile range (IQR), line indicates median, and whiskers denote ±1.5 × IQR. The bar plot represents the average median fluorescence intensity (MFI) ± SD of two different guides targeting the same gene ($n = 4$ per condition, $^{****}P < 0.0001$ by one-way ANOVA with Tukey's post hoc test).

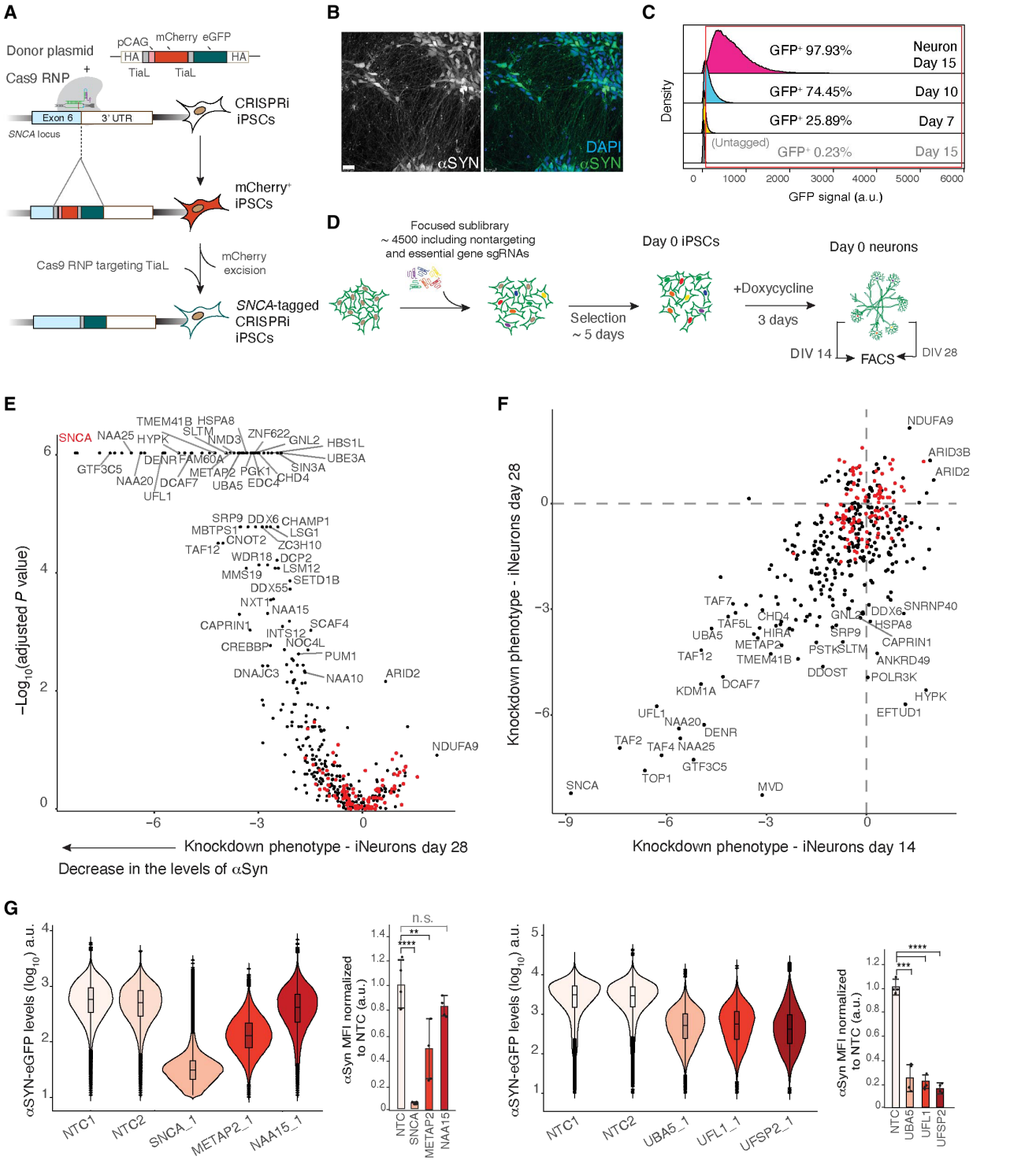

Fig. 2. Targeted CRISPRi screen in *SNCA*-tagged iNeurons identifies gene hits that affect neuronal αSyn levels. (**A**) Schematic showing the strategy used to tag the C terminus of *SNCA* with monomeric enhanced GFP in CRISPRi-iPSCs. (**B**) Validated single clones were differentiated into iNeurons using doxycycline induction. The DIV14 iNeurons were analyzed for GFP expression using confocal microscopy. Scale bar, 20 μM. (**C**) GFP fluorescence was measured in the iNeurons derived from validated *SNCA*-tagged CRISPRi-iPSC clones at the indicated lengths of differentiation using flow cytometry to demonstrate a neuronal maturation–dependent increase in the levels of αSyn-GFP. (**D**) Illustration of the CRISPRi secondary pooled screen to identify αSyn regulators in iNeurons. (**E**) Volcano plot displaying the phenotypes and the significance of hits influencing αSyn in DIV28 iNeurons. (**F**) Comparison of gene phenotypes between days 14 and 28 iNeurons. (**G**) Flow cytometry–based quantification of αSyn expression levels in DIV15 iNeurons following CRISPRi-based KD of different negative modulators identified in the screen as shown. Violin plots represent the GFP fluorescence intensity distribution of iNeurons derived from *SNCA*-tagged iPSCs from two independent cultures. The bar plot represents the average MFI ± SD of two different guides targeting the same gene ($n = 4$ per condition, $^{**}P < 0.01$, $^{***}P < 0.001$, and $^{****}P < 0.0001$, one-way ANOVA with Tukey's post hoc test. n.s., not significant).

Analysis of protein-protein interactions using the STRING database (https://string-db.org/) of the top positive regulators of αSyn in the SKMEL30 cells revealed two main clusters: KDM1A-ZNF217 and a small cluster of RNA binding proteins including the well-studied stress granule protein G3BP1 (Fig. 3A). As none of these proteins came up as hits in the neuronal screen, we asked whether this was due to cell type–specific regulation, effects of KD on neuronal differentiation, or lower sensitivity to smaller effect sizes in the neuronal screens. KDM1A (LSD1) is a well-characterized neuronal epigenetic regulator (*28*) that has been previously shown to interact with ZNF217 (*29*). Because down-regulation of KDM1A can affect neuronal differentiation (*25*), we asked whether inhibiting KDM1A after differentiation would result in an opposite phenotype, similar to what we observed in our primary screen. Treatment of iNeurons on day 7 after differentiation(DIV7) with a KDM1A inhibitor (GSK-LSD1)

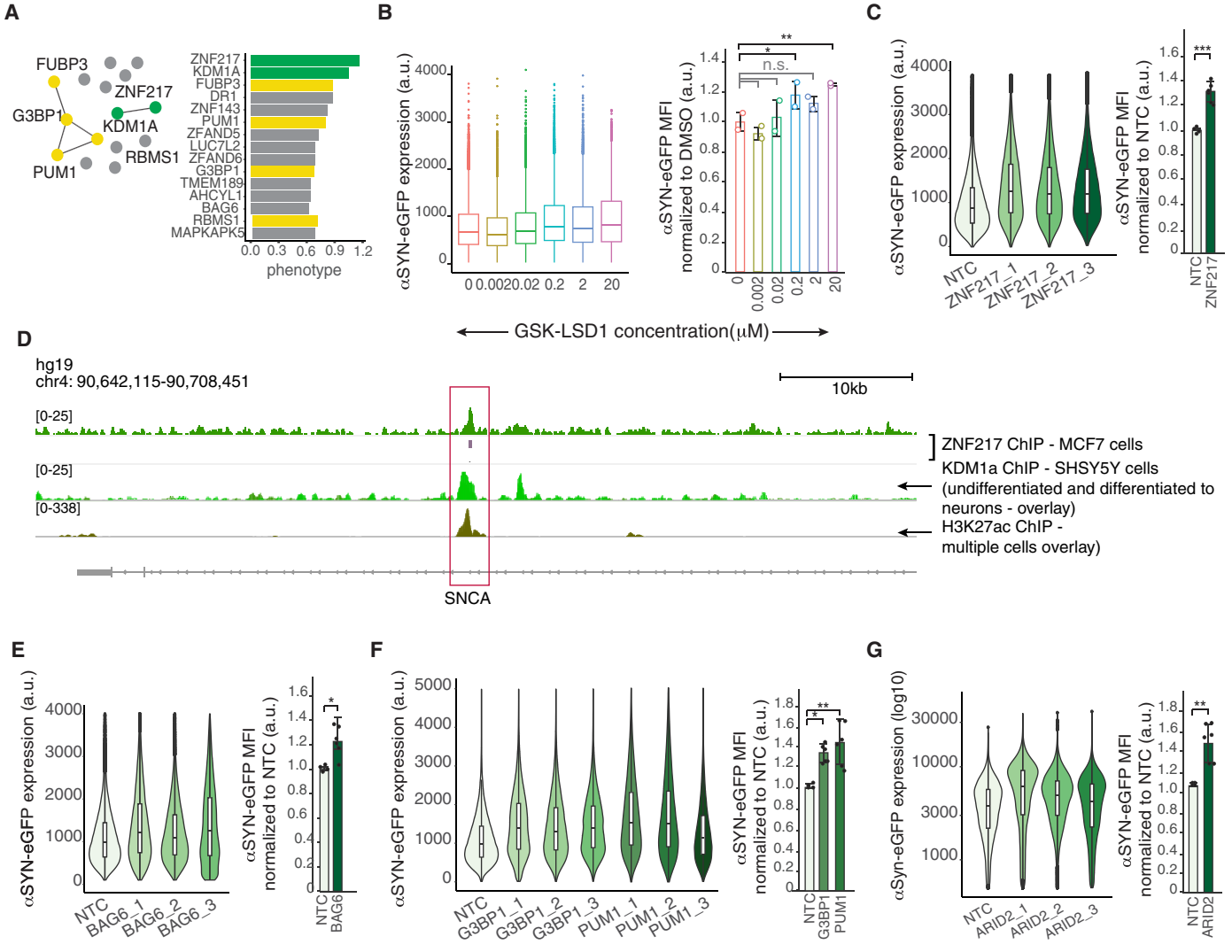

Fig. 3. Cell line and neuronal screen identifies repressors of αSyn. (**A**) Protein-protein interaction network for the top gene hits that increased levels of αSyn in the SKMEL30 screen based on STRING analysis. Solid lines indicate direct interaction, and the bar plot on the right shows the phenotype (increasing levels of αSyn) associated with genes displayed in the clustering analysis. (**B**) Flow cytometry–based quantification of the dose-dependent effect of GSK-LSD1 on αSyn expression levels in *SNCA*-tagged iNeurons. The bar plot represents the average MFI ± SD of two independent neuronal cultures for a given dose (*$P < 0.05$ and **$P < 0.01$, one-way ANOVA with Tukey's post hoc test. n.s., not significant). (**C** and **E** to **G**) Flow cytometry–based quantification of αSyn expression levels in iNeurons following CRISPRi-based KD of different positive modulators as shown. iNeurons were transduced with NTC guides or guides targeting (C) ZNF217; (E) BAG6; (F) G3BP1 and PUM1; and (G) ARID2. Violin plots represent the GFP fluorescence intensity distribution of iNeurons derived from *SNCA*-tagged iPSCs from two independent cultures. The bar plot represents the average MFI ± SD of three different guides targeting the same gene ($n = 6$ per condition, *$P < 0.05$, **$P < 0.01$, and ***$P < 0.001$, one-way ANOVA with Tukey's post hoc test). (**D**) ChIP-seq data (*28*, *30*) for the zinc-finger protein, ZNF217, in MCF-7 breast cancer cells and for KDM1a in undifferentiated SH-SY5Y and SH-SY5Y cells differentiated to neurons (overlay), respectively, showing signals in the intron 4 region of the *SNCA* gene. The identified peak for ZNF217 is indicated as a gray bar below the ChIP-seq signal. Also showing the browser views of overlaid H3K27ac mark: CHIP-seq enrichment at *SNCA*, data of five different cell types obtained from the Encyclopedia of DNA Elements (ENCODE). Genomic coordinates and human RefSeq annotations for the *SNCA* gene are shown.

revealed a dose-dependent increase in the αSyn protein levels (Fig. 3B and fig. S3B).

KD of ZNF217 did not affect differentiation and yet did not appear as a top hit in our neuronal screen. Regardless, we tested the effect of ZNF217-KD in iNeurons and observed a significant increase in αSyn protein levels (Fig. 3C). To lend additional support to the role of these two proteins in the repression of αSyn protein levels, we mined publicly available chromatin immunoprecipitation sequencing (CHIP-seq) data (*28*, *30*) and found that both proteins physically bind the fourth intron of the *SNCA* gene at the precise same region (Fig. 3D). We also observed strong enrichment of histone 3 lysine 27 acetylation (H3K27ac) signals at the same position in a wide variety of cell lines (Fig. 3D and fig. S3C), suggesting a possible mechanism by which KDM1A/ZNF217 can regulate *SNCA* transcription through histone acetylation. KDM1A inhibitors are considered for several cancer clinical trials (*31*, *32*), and it might be worth evaluating how these inhibitors affect αSyn expression levels.

We individually validated a set of additional hits from our primary screen: RNA binding proteins (Fig. 3A, yellow cluster) such as G3BP1 and PUM1, and BAG6, a cytosolic chaperone (*33*). We also examined the genes that stood out in our neuronal screen for increased αSyn levels, such as *ARID2*. In all cases, we found a significant increase in endo-αSyn levels in iNeurons (Fig. 3, E to G). *ARID2* resides in proximity with a PD-risk locus (*34*), suggesting that it may act by affecting αSyn protein levels. Overall, performing screens in more than one cell type, especially a cell line that is not susceptible to effects on differentiation, results in a more comprehensive exploration of the gene modifier networks.

CRISPRi and CRISPR-KO screen results converge to reveal NTA enzymes as major modifiers of αSyn levels irrespective of the cell type

We next sought to generate a list of genes that are crucial for sustaining αSyn levels across the two cell types by comparing the top gene hits from our SKMEL30 screen to the hits recovered from the neuronal CRISPRi screen. Despite using two different cell lines and gene perturbation methods, we were able to identify a large subset of genes that regulated αSyn in a cell type–independent manner (Fig. 4A). Among these were some PD-risk genes (e.g., *NMD3*), αSyn interactors (e.g., HYPK and CTNNB1), modifiers of αSyn expression levels (e.g., SRP9) or aggregation (e.g., NAA25), and genes that exhibited differential expression in patients with PD (e.g., *HBS1L*) (full list of genes and references is presented in table S4). To gain insight into the different pathways contributing to the reduction in αSyn levels, we clustered the gene hits from both screens using the STRING database (*35*). This analysis highlighted sets of genes at different regulatory layers, from transcription to posttranslational protein modifications (Fig. 4B and fig. S1G). Notably, one of the clusters contained genes involved in mRNA decapping and decay (e.g., *EDC4* and *DDX6*), further supporting a recently suggested role for αSyn integration into the decapping module of processing bodies (*36*). We also identified several genes belonging to the Ubiquitin Fold Modifier 1 (UFM1) cascade (e.g., *UBA5*, *UFSP2*, and *UFL1*; Fig. 2G) (*37*), suggesting an interesting link between this unique posttranslational modification and αSyn levels.

Several proteins in the NTA pathway stood out from other regulators in their effect sizes in both cell types (Fig. 4, A and B), so we decided to further investigate their underlying mechanism and therapeutic potential. NTA is an irreversible protein modification that involves the enzymatic addition of an acetyl group to the N-terminal amino acid of a growing polypeptide chain (*38*) or a mature protein (*39*). This widespread modification, known to be mediated by a group of enzymes (NatA to NatF and NatH), can affect multiple aspects of the protein, including stability, folding, localization, and complex formation (*38*). All three secondary screens identified *NAA25* and *NAA20* as the major negative regulators of αSyn, after *SNCA* itself (Figs. 4A, 2F, and 1G). *NAA25* and *NAA20* are genes that encode the auxiliary and catalytic subunits of the human NatB, which acetylates the initiator methionine of αSyn in vivo (*40*, *41*). NTA of αSyn in vivo is well documented (*40*), yet the precise roles of this modification are still being investigated. NTA of αSyn was shown to affect the lipid binding and aggregation properties of αSyn (*42*–*44*) in solution. A recent study implicated the effect of NTA on the stability and toxicity of αSyn using exogenously expressed variants but with some conflicting results from a previous similar study (*45*, *46*).

Hence, to thoroughly study the role of this modification in αSyn regulation, we first validated our screen results by silencing the auxiliary subunit of the NatB complex, *NAA25*, in iNeurons and measured the endo-αSyn using three orthogonal approaches (Fig. 4, C to E). Arrayed delivery of sgRNAs targeting *NAA25* in both *SNCA*-tagged (Fig. 4C) and parental untagged CRISPRi-iN iPSC lines (Fig. 4, D and E, and fig. S4A) showed a marked reduction in endo-αSyn levels, with minimal apparent toxicity, suggesting that nonacetylated αSyn (hereby referring to endo-αSyn that lacks NTA) is rapidly degraded in iNeurons.

While 20% of the human proteome is predicted to be modified by NatB, down-regulation of NatB subunits in yeast (*47*, *48*) and mammalian cells (*49*) only marginally affects the levels and stability of its substrate proteins. This can be partly explained by the observation that an efficient KD (more than 85%) of the NatB subunit is required to completely deplete its substrate proteins of this modification (*49*). To test whether this was also the case in our neuronal model, we performed quantitative proteomics in iNeurons following CRISPRi-mediated repression of NAA25 using label-free mass spectroscopy, followed by differential protein expression analysis (Fig. 4F). Analogous to the previous observation, modest repression of NAA25 did not influence the expression of most of the NatB substrates (predicted on the basis of the canonical NatB substrate recognition sequence), including a closely related family member, γ-synuclein (*SNCG*). However, this reduction in NAA25 was sufficient to markedly lower levels of αSyn in iNeurons (Fig. 4E). Notably, the reduction in αSyn levels that we observed in the proteomics data was lesser than the actual effect observed by immunoblotting (Fig. 4E and fig. S4A), most likely due to the low peptide coverage of αSyn in this dataset (table S5).

Nonacetylated αSyn is targeted for degradation by the proteasome in a Ube2w-dependent manner

Although NTA has been shown to enhance the stability of select proteins, a recent study reported a lack of correlation between the NTA status of proteins and their turnover (*50*, *51*). Conflictingly, the acetyl group can also act as a degron in some cases (*52*). Thus, we set out to further investigate the functional role of this modification on the stability and degradation of αSyn. The rapid loss of endo-αSyn in NAA25-deficient cells impeded our mechanistic exploration of αSyn stability. Hence, we designed a set of αSyn mutants that would allow us to systematically change the NTA status of αSyn by

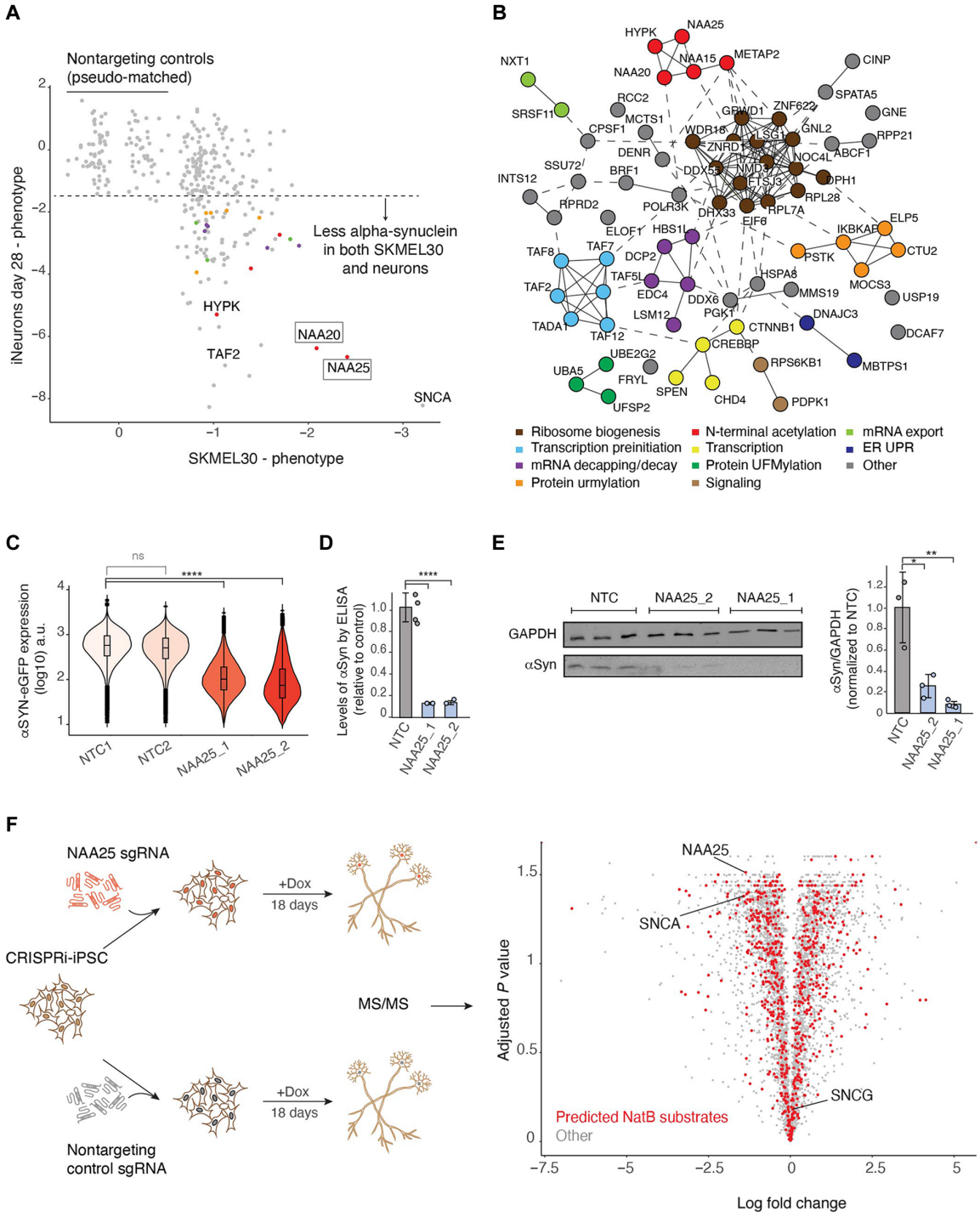

Fig. 4. Comparison of the two screens identifies shared hits and highlights the importance of the NTA pathway. (**A**) Comparison of phenotype between the CRISPR-KO screen performed in SKMEL30 (*x* axis) and the CRISPRi screen in DIV 28 iNeurons (*y* axis). Each dot represents a gene, the depletion of which resulted in decreased levels of αSyn in both screens. Genes are color-coded based on the functional groups as shown in the STRING analysis. (**B**) Protein-protein interaction (STRING database) clustering for a selective list of genes, which, when knocked down, lead to reduced αSyn protein levels in iNeurons. (**C**) Flow cytometry–based quantification of αSyn expression levels in iNeurons derived from *SNCA*-tagged CRISPRi-iPSCs following KD of the auxiliary subunit of NatB, NAA25. ($n = 2$, $^{****}P < 0.0001$, one-way ANOVA with Tukey's post hoc test. n.s., not significant). (**D** and **E**) αSyn expression levels in iNeurons (DIV15) derived from untagged CRISPRi-iPSCs following KD of NAA25 were measured using (D) ELISA [NTC ($n = 4$); samples ($n = 2$), $^{****}P < 0.0001$, one-way ANOVA with Tukey's post hoc test. Data are absolute levels of αSyn normalized to NTC iNeurons ± SD] and (E) immunoblot for αSyn. Data are mean αSyn/GAPDH levels normalized to NTC ± SD from three independent neuronal cultures ($n = 3$, $^{*}P < 0.05$ and $^{**}P < 0.01$, one-way ANOVA with Tukey's post hoc test). (**F**) Label-free MS experiment was performed to quantify proteins that change in iNeurons derived from CRISPRi-iPSCs following the KD of NAA25. The red dots mark proteins that are possible NatB substrates based on the first two amino acids.

mutating the second amino acid: αSyn^{D2R} and αSyn^{D2Y} block acetylation by NatB and instead favor lower acetylation recognition by NatE (*53*), and αSyn^{D2E} preserves the NatB recognition sequence (serving as a positive control). We overexpressed αSyn^{WT} and αSyn^{D2R} in human embryonic kidney (HEK) 293T cells and used matrix-assisted laser desorption/ionization–time-of-flight (MALDI-TOF) mass spectrometry (MS) on the immunoprecipitated proteins to reveal the NTA status. While only a single peak corresponding to acetylated αSyn was present in αSyn^{WT} (fig. S5A), we observed a mixed population of acetylated and nonacetylated αSyn in the αSyn^{D2R} variant (Fig. 5A), indicating that the αSyn^{D2R} mutation directly impaired NTA of αSyn as expected. To estimate the level of NTA reduction in the αSyn^{D2R} mutant, we generated a standard curve using mixtures of quantifiable concentrations of recombinant N-terminally acetylated and nonacetylated αSyn, followed by MALDI-TOF (fig. S5, B to D). We then used this standard curve to quantify the levels of N-terminally acetylated αSyn immunoprecipitated from HEK293T cells. As expected, αSyn^{WT} was completely N-terminally acetylated, while αSyn^{D2R} exhibited a mixed population of acetylated and nonacetylated αSyn proteins, showing approximately a 51% decrease in acetylated protein (Fig. 5A). Transduction of αSyn^{WT} and mutants (αSyn^{D2R} and αSyn^{D2E}) into NAA25-deficient and wild-type iNeurons confirmed that the expression level of αSyn in wild-type iNeurons expressing αSyn^{D2E} remains unaffected, suggesting that the mutant is still being acetylated by NatB in vitro (fig. S5E).

We next lentivirally introduced the mutants (αSyn^{WT}, αSyn^{D2R}, and αSyn^{D2E}) in *SNCA*-KD iNeurons and evaluated the effect of NTA and its loss on the levels of αSyn using Western blot. iNeurons expressing the αSyn^{D2R} mutant effectively recapitulated the phenotype observed in *NAA25*-KD iNeurons with an almost undetectable expression level of αSyn. Meanwhile, αSyn levels in iNeurons expressing αSyn^{D2E} remained unaffected compared to αSyn^{WT} (Fig. 5B). We observed similar results in HEK293T cells in which we were able to achieve slightly higher levels of mutant αSyn expression, therefore making them more suitable for follow-up mechanistic exploration (fig. S5F). The αSyn^{D2Y} mutant showed an impairment in protein expression similar to αSyn^{D2R} (fig. S5G), suggesting that the αSyn instability was not induced because of the charge change from negative (Asp) to positive (Arg). We next assessed the stability of αSyn^{WT} and αSyn^{D2R} expressed in HEK293T cells using cycloheximide (Chx) chase experiments. While endo-αSyn turnover was comparable between the two conditions, we observed that loss of NTA in the αSyn^{D2R} mutant was sufficient to increase the turnover of the partially N-terminally acetylated protein ($t_{1/2}$ = 4 hours) compared to the fully N-terminally acetylated wild-type protein ($t_{1/2}$ = 15 hours) (Fig. 5C). These experiments demonstrate that nonacetylated αSyn is rapidly degraded in neuronal cells and that this modification is essential for αSyn stability.

Given the rapid depletion of nonacetylated αSyn, we assessed the degradation of αSyn mutants by treating SKMEL30 cells stably expressing αSyn^{WT}-eGFP or αSyn^{D2R}-eGFP with inhibitors targeting

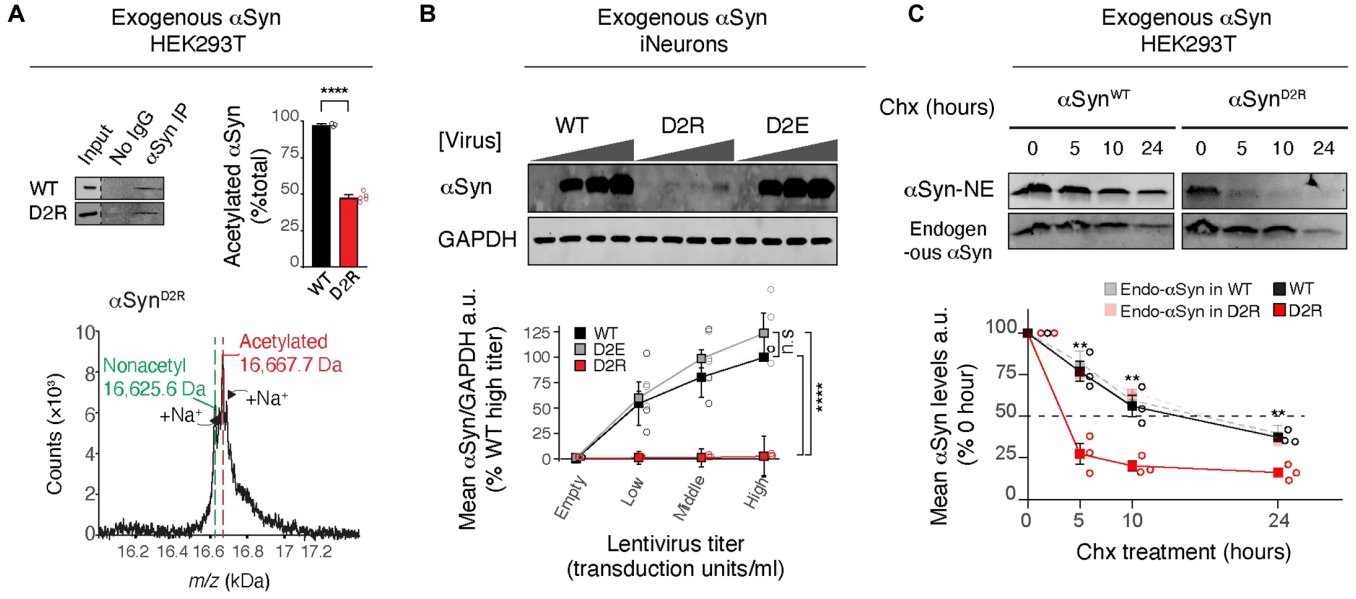

Fig. 5. NTA is essential for the stability of αSyn. (**A**) HEK293T cells, transfected with either αSyn^{WT} or αSyn^{D2R} constructs, were lysed 48 hours after transfection for anti-αSyn IP. The eluate was subjected to SDS-PAGE followed by anti-αSyn immunoblot. No IgG = IP without antibody (control). IP, immunoprecipitation. Loss of acetylation was detected in αSyn^{D2R} (n = 5 independent IPs) by MALDI-TOF MS. The masses were as follows: αSyn^{D2R}: nonacetylated (predicted 16,625.33 Da; actual 16,625.6 Da); acetylated (predicted 16,667.33 Da; actual 16,667.7 Da). Met-cleaved αSyn was not detected (16,476.12 Da for αSyn^{D2R}). The percentage of acetylation, measured using quantitative MALDI-TOF MS, is represented using the bar plot. The calculation for quantitative MALDI-TOF MS can be found in fig. S4. *m/z*, mass/charge ratio. (**B**) Western blot analysis of αSyn levels in *SNCA* KD iNeurons transduced with either SNCA^{WT}, SNCA^{D2R}, or SNCA^{D2E} at equal MOIs at increasing titer levels and harvested 14 days after transduction. Data represent the levels of αSyn normalized to levels of GAPDH quantified using Western blot, n = 3 independent cultures and transductions, error bars indicate ±SD, ****P < 0.0001 by one-way ANOVA with Tukey's post hoc test. n.s., not significant. (**C**) Turnover of αSyn^{WT} and αSyn^{D2R} was measured by Chx chase in HEK293T cells transduced with either construct. Five days after transduction, cells were treated with 25 μM Chx for the indicated time points (5, 10, and 24 hours). The faded dashed lines represent the turnover of endo-αSyn (control) in either sample group. Immunoblots are each representative of n = 3 independent transductions and experiments. **P < 0.01, by one-way ANOVA with Tukey's post hoc test.

lysosomal proteases and proteasomes for 24 hours: 50 μM chloroquine (an autophagy-lysosome inhibitor), 500 nM MG132, and 500 nM epoxomicin (proteasome inhibitors). Ectopic expression of eGFP-fused αSyn variants enabled easy monitoring of αSyn degradation using flow cytometry. We observed that the αSyn^{D2R}-eGFP variant resisted degradation efficiently in the presence of proteasome inhibitors, MG132, and epoxomicin, but not in the presence of chloroquine (Fig. 6A and fig. S6A). Thus, our study demonstrates that nonacetylated αSyn is targeted for degradation by the proteasome and not the lysosome.

We next sought to investigate the mechanisms by which nonacetylated αSyn is degraded. A recent in vitro study with human recombinant αSyn reported that αSyn can be ubiquitinated by Ube2w (*54*), an E2 enzyme known to N-terminally ubiquitinate proteins with disordered N termini (*55*). These findings raise the possibility that endo-αSyn in the absence of NTA is actively targeted for ubiquitin-dependent degradation by the encoded Ube2w enzyme. We therefore hypothesized that nonacetylated αSyn can be rescued from degradation by silencing *UBE2W*. We tested this hypothesis by generating double KDs in iNeurons (*NAA25* + *UBE2W* KD). We observed that endo-αSyn levels in NAA25 + Ube2w–deficient iNeurons were significantly higher compared to NAA25 + NTC iNeurons, suggesting that nonacetylated αSyn was partially protected from degradation following Ube2w repression (Fig. 6B). Together, we conclude that NTA acts as a major determinant of αSyn stability: αSyn lacking NTA is prone to degradation by proteosomes, which can be rescued by silencing Ube2w in iNeurons. Whether there is a direct interaction between Ube2w and nonacetylated αSyn and whether this interaction mediates N-terminal ubiquitination or other Ube2w-related posttranslational modifications (*56*) will require further investigation.

Loss of NTA leads to rapid degradation of cytosolic αSyn

Protein turnover of cytosolic proteins is typically regulated by the ubiquitin-proteasome system, whereas membrane-bound proteins generally rely on the endolysosomal degradation pathway (*57*). In neurons, αSyn exists as two pools: a disordered cytosolic form and a helix-rich membrane-bound form, and the equilibrium between these two populations is tightly regulated (*58*). The increased sensitivity of nonacetylated αSyn to proteasome-mediated degradation led us to evaluate the distribution of αSyn occupying the cytosolic and membrane fractions in iNeurons (Fig. 7, A and B) and in HEK293T cells (fig. S7A). To analyze the subcellular distribution of αSyn, we performed ultracentrifugation-based subcellular fractionation to

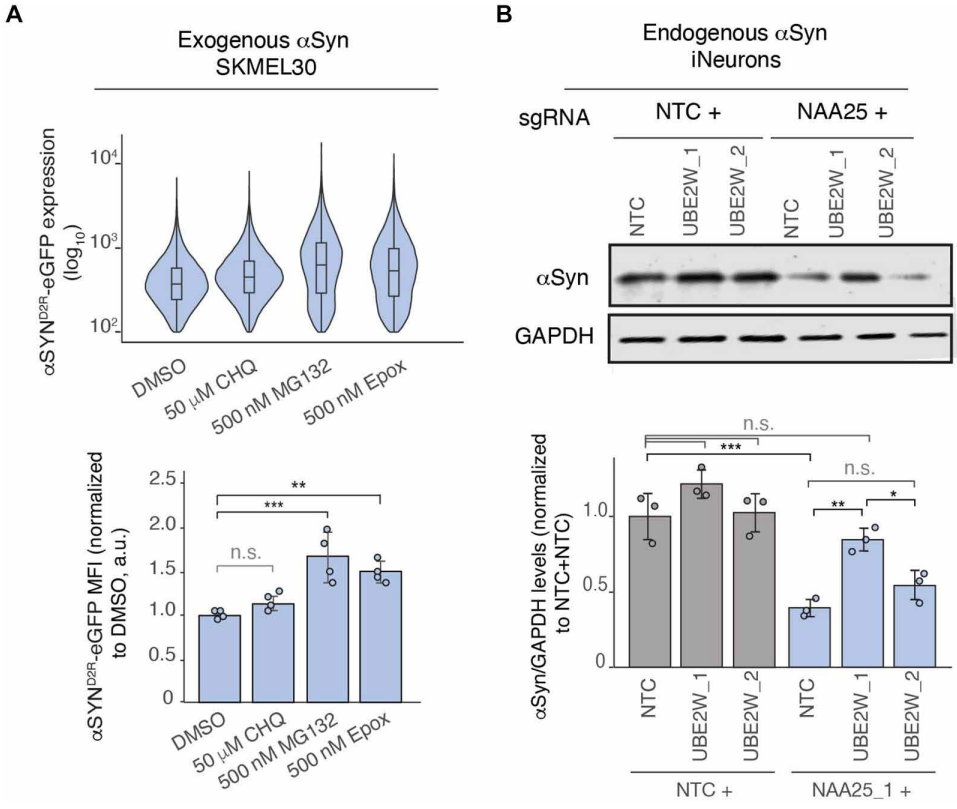

Fig. 6. Degradation of nonacetylated αSyn by the proteasomes is rescued by knocking down the N-terminal ubiquitinating enzyme, Ube2w. (**A**) SKMEL30 melanoma cells, transduced with either αSyn^{WT}_GFP or αSyn^{D2R}_GFP constructs, were treated with DMSO, chloroquine (50 μM), MG132 (500 nM), or epoxomicin (500 nM) for 24 hours, showing that the nonacetylated αSyn^{D2R} construct is degraded by the proteasome. The GFP levels measured using flow cytometry are represented using violin plots. The bar plot represents the average MFI normalized to DMSO ± SD ($n = 4$ per condition, $^{**}P < 0.01$ and $^{***}P < 0.001$, one-way ANOVA with Tukey's post hoc test. n.s., not significant). (**B**) Western blot analyses of endo-αSyn from DIV15 iNeurons with double gene KD expressing either NTC sgRNA or *NAA25* sgRNA with and without *UBE2W* sgRNAs. GAPDH was used as a loading control. Data represent the levels of αSyn/GAPDH normalized to NTC + NTC iNeurons quantified using Western blot, $n = 3$ independent culture per sample, error bars indicate ±SD, $^{*}P < 0.05$, $^{**}P < 0.001$, and $^{***}P < 0.0001$ by one-way ANOVA with Tukey's post hoc test. n.s., not significant.

separate membrane and cytosolic cellular fractions and measured the levels of αSyn present in the two fractions. Despite a reduction in the overall levels of αSyn, we found a preferential reduction in the cytosolic population compared to the membrane-bound population in the iNeurons expressing αSyn^{D2R}. In contrast, neither population was affected by the αSyn^{D2E} mutation in iNeurons.

Because of the extremely low expression levels of the αSyn^{D2R} mutant in iNeurons, we performed a similar experiment using *NAA25*-deficient iNeurons (with modest NAA25 KD) to measure the subcellular distribution of endo-αSyn. These measurements revealed a preferential depletion of endo-αSyn from the cytosol but not in the membrane-bound pool (Fig. 7B), and these findings were also confirmed in HEK293T cells overexpressing either αSyn^{WT} or αSyn^{D2R} (fig. S7A). We further confirmed that the αSyn^{D2R} mutant did not have reduced solubility compared to αSyn^{WT} using a Triton X-100 solubility assay (fig. S7B), ruling out the possibility that the observed loss of cytosolic nonacetylated αSyn is a consequence of faster degradation of membrane-bound αSyn coupled with reduced solubility of the αSyn^{D2R} mutant.

To further resolve the subcellular distribution of αSyn in the absence of NTA, we performed microscopy on *SNCA*-KD iNeurons transduced with either αSyn^{WT}, $\alpha Syn^{D2R,}$ or αSyn^{D2E} and aged them for 100 days to allow for synaptic maturation. αSyn signal was markedly absent from the soma in αSyn^{D2R} but not in αSyn^{WT} and αSyn^{D2E} (fig. S7C), which both showed distributions similar to the endo-αSyn (Fig. 2B). Meanwhile, presynaptic localization of αSyn^{D2R} was retained as measured by colocalization with the presynaptic protein synapsin1, suggesting that the membrane-bound mutant protein was more stable compared to the depleted somatic αSyn protein. Overall, these findings led us to conclude that NTA of αSyn specifically protects the cytosolic pool from degradation.

Studies have reported the importance of NTA in driving the α-helical formation of αSyn at its N terminus (*59*). This region, along with a membrane-anchor domain and the unstructured C-terminal region, dictates the membrane localization of αSyn (*60*). As we observed little to no difference in the membrane-bound αSyn fraction in the absence of NTA, we further investigated the acetylation status of αSyn^{D2R} in the cytosolic and membrane fractions using MALDI-TOF (Fig. 7C and fig. S7D). We detected a greater peak for nonacetylated αSyn in the cytosol compared to the membrane fraction, suggesting that NTA promotes the membrane association of αSyn in cells. These data indicate that decreasing NTA affected the subcellular distribution of αSyn by reducing the binding of αSyn to membranes, with the cytosolic αSyn pool being more susceptible to degradation via loss of NTA than the membrane-bound pool.

METAP2 inhibition reduces endo-αSyn in iNeurons carrying *SNCA* triplication

While the loss of NatB-complex genes had the strongest effect on αSyn protein levels, we also identified additional genes associated with NTA, such as *NAA15*, *HYPK*, and *METAP2*, as modifiers in our screen (Fig. 3, A and B). Members of other Nat complexes, such as NatC, did not score as gene hits (Fig. 8A). We first validated the

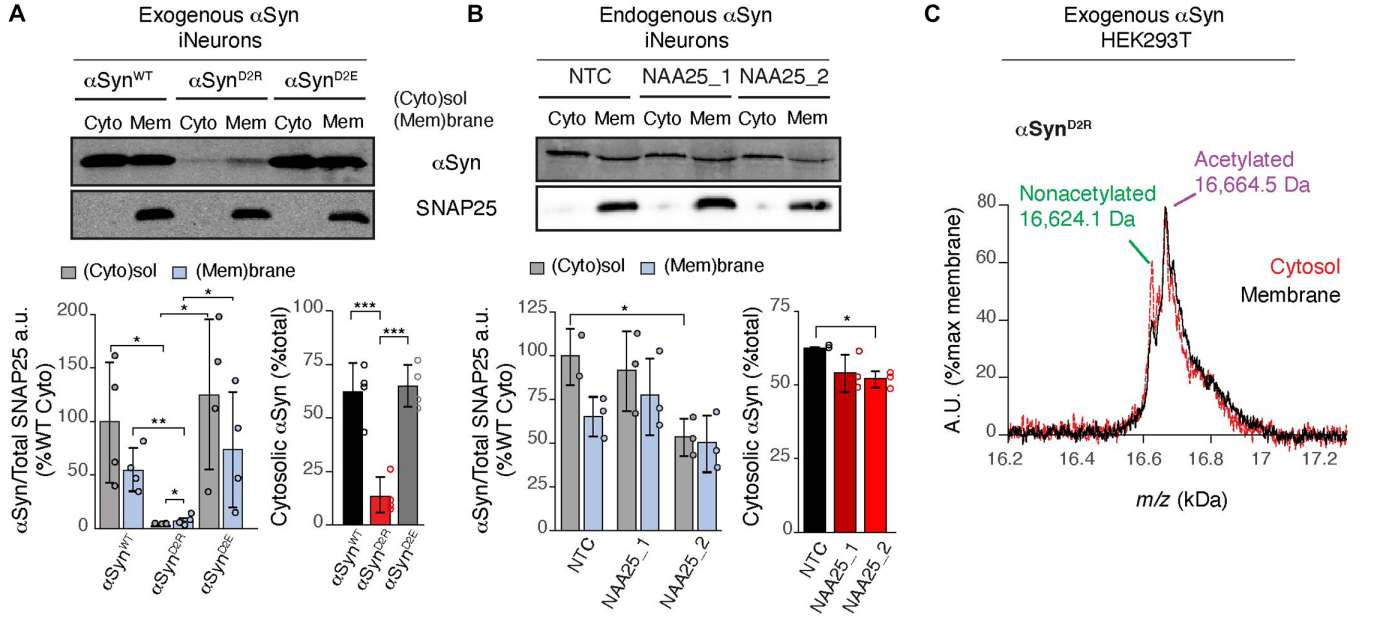

Fig. 7. Loss of NTA leads to preferential depletion of cytosolic αSyn. (**A** and **B**) Western blot analysis of αSyn levels in (A) *SNCA* KD iNeurons derived from CRISPRi-iPSCs transduced with either $SNCA^{WT}$, $SNCA^{D2R}$, or $SNCA^{D2E}$ or (B) iNeurons transduced with sgRNAs targeting *NAA25* or NTC and harvested 4 weeks later for membrane-cytosol fractionation. SNAP-25 was used to confirm membrane separation from the cytosol. (A) $n = 4$ independent cultures and transductions per sample, $^*P < 0.05$ and $^{***}P < 0.0001$ by one-way ANOVA with Tukey's post hoc test. (B) $n = 3$ independent cultures per sample. $^*P < 0.05$ by one-way ANOVA with Tukey's post hoc test. All data represent mean ± SD. (**C**) Membrane and cytosolic fractions were separated from transfected HEK293T cells expressing either αSyn^{D2R} or αSyn^{WT}. αSyn was immunoprecipitated separately from each fraction and analyzed using MALDI-TOF for acetylated and nonacetylated αSyn. Nonacetylated αSyn was less likely to be found in the membrane fraction. Data points were normalized to the maximum data point in the membrane fraction. Peaks were detected at αSyn^{WT}: nonacetylated (predicted 16,584.23 Da; not detected); acetylated (predicted 16,626.23 Da; actual 16,626.8 Da). αSyn^{D2R}: nonacetylated (predicted 16,625.33 Da; actual 16,624.1 Da); acetylated (predicted 16,667.33 Da; actual 16,664.5 Da). The spectra were measured by pooling together $n = 3$ independent transfections and independent IPs before MALDI-TOF.

effect of NAA15, the enzymatic subunit of the NatA complex, and METAP2, a cytosolic enzyme involved in the cleaving of initiator methionine, in both *SNCA*-tagged and untagged iNeurons and measured the αSyn abundance using Western blotting and flow cytometry (Fig. 8B and fig. S8, A and B). Consistent with our screen results, down-regulation of NAA15 and METAP2 resulted in a decrease of αSyn in iNeurons. We decided to further explore the mechanism of METAP2 regulation of αSyn for two main reasons: (i) METAP2 is required for the proper assembly of the NatB complex (*61*), and (ii) several METAP2 inhibitors have been used in clinical trials, including TNP470, that can penetrate the blood-brain barrier (*62*). While cell-permeable inhibitors targeting NAA25 or the NatB complex are currently unavailable, we decided to repurpose currently available METAP2 inhibitors to indirectly down-regulate αSyn levels in iNeurons by modulating NatB subunit expression. In alignment with previous findings (*61*), in which METAP2 was demonstrated to be a central regulator of NatB subunit expression and complex formation, we hypothesized that silencing METAP2 should negatively affect NAA25 expression levels, which, in turn, should attenuate levels of αSyn. First, we confirmed that knocking down METAP2 resulted in the reduction of NAA25 levels in iNeurons using a Western blot (Fig. 8C). We also confirmed a subtle reduction in the expression levels of NAA20 in HEK293 cells lacking METAP2 (fig. S8C). Next, we sought to test whether pharmacological inhibition of METAP2 could negatively affect αSyn levels in iNeurons.

Several METAP2 inhibitors have been tested for cancer and obesity in clinical trials (*63*, *64*); of these, we specifically chose TNP470 because of its ability to penetrate the blood-brain barrier. We first tested whether the drug can effectively lower αSyn in human iNeurons derived from *SNCA*-tagged iPSCs. We treated DIV7 neurons for 14 days and measured αSyn levels using flow

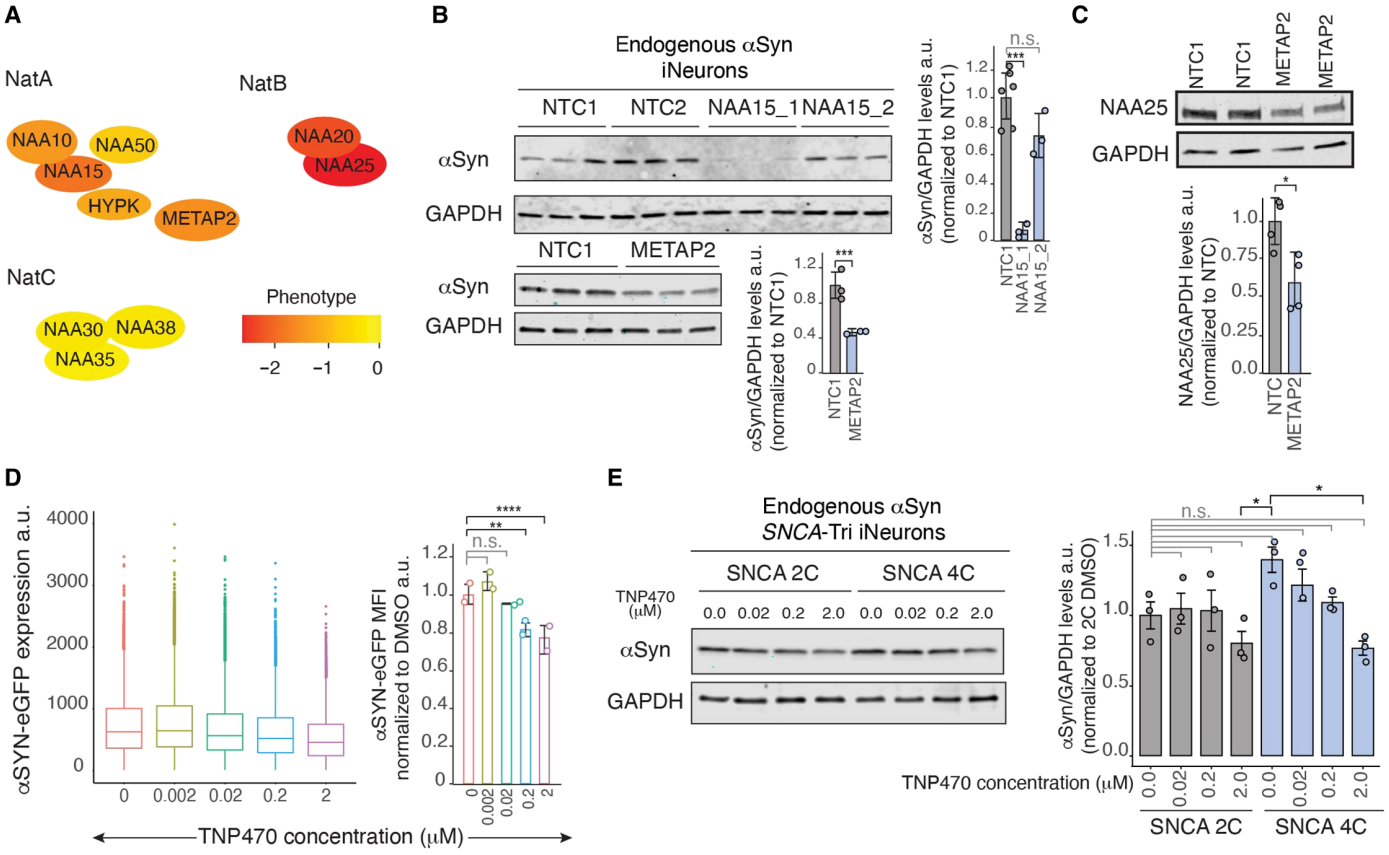

Fig. 8. Genetic and pharmacological perturbation of METAP2 leads to decreased αSyn levels in iNeurons. (**A**) Heatmap depicting the effects of knocking out different subunits of the major NAT complexes on levels of αSyn in SKMEL30s. (**B**) Western blot analysis of endo-αSyn levels in DIV15 iNeurons derived from CRISPRi-iPSCs transduced with the indicated sgRNAs (NTC, nontargeting control). All data mean αSyn/GAPDH levels ± SD. NAA15 blot: NTC ($n = 6$), NAA15 guides ($n = 3$ independent cultures per sample). ***$P < 0.0001$ by one-way ANOVA with Tukey's post hoc test. METAP2 blot: $n = 3$ independent cultures per sample, ***$P < 0.0001$ by Student's t test. (**C**) Western blot analysis of NAA25 levels in METAP2 KD iNeurons derived from CRISPRi-iN iPSCs and harvested on DIV15 for immunoblot. $N = 4$ independent cultures per sample. *$P < 0.05$, by Student's t test. All data represent mean αSyn/GAPDH ± SD. (**D**) Flow cytometry–based quantification of the dose-dependent effect of TNP470 on αSyn expression levels in *SNCA*-tagged iNeurons. DIV7 iNeurons were treated with different concentrations of TNP470, a small-molecule inhibitor targeting METAP2, for 14 days. The bar plot represents the average MFI ± SD of two independent neuronal cultures for a given dose ($n = 2$, **$P < 0.01$ and ***$P < 0.001$, one-way ANOVA with Tukey's post hoc test. n.s., not significant). (**E**) Western blot analysis of endo-αSyn protein levels in PD patient iPSC-derived iNeurons carrying four copies of *SNCA* (4C, blue) and isogenic controls carrying two copies of *SNCA* (2C, gray) treated with various doses of TNP470. Data represent the levels of αSyn/GAPDH normalized to DMSO-treated 2C-iNeurons quantified using Western blot, $n = 3$ independent cultures and treatments per sample group, error bars indicate ±SD, *$P < 0.05$ by one-way ANOVA with Tukey's post hoc test. n.s., not significant.

cytometry. We observed a dose-dependent decrease in the levels of αSyn in iNeurons treated with TNP470 (Fig 8D and fig. S8D). We then tested the efficacy of the drug in a disease-relevant context by turning to iNeurons derived from patients with familial PD harboring the *SNCA* triplication locus (*SNCA* 4C) and an isogenic control corrected for *SNCA* copy number (*SNCA* 2C). DIV7 iNeurons derived from both iPSCs were treated with different amounts of TNP470, and αSyn levels were measured after 14 days of treatment using Western blot (Fig. 8E). PD patient–derived iNeurons carrying *SNCA* triplication showed a greater reduction in the levels of αSyn compared to isogenic control lines, especially at lower drug concentrations. This result is in line with the strong dependency of αSyn on NatB activity levels and suggests that METAP2 inhibitors might have therapeutic potential for lowering αSyn levels in the brain.

DISCUSSION

Decades of research into PD and related synucleinopathies have pointed to a central role of αSyn in disease pathogenesis. Many ongoing therapeutic strategies aim at targeting αSyn proteins either directly or reducing their levels by targeting transcription or the mRNA (*65*). Despite the importance of αSyn biology and protein levels, the precise genetic networks that regulate endo-αSyn levels remain poorly understood. This is mainly due to the fact that αSyn expression is restricted to certain cell types (*66*, *67*), forcing screening efforts to rely on artificial overexpression (*11*, *12*). Here, we identified a melanoma cell line with naturally high αSyn levels and engineered the *SNCA* locus to insert a fluorescent tag after the last exon. We also generated an iPSC-reporter cell line that allowed us to measure the abundance of endo-αSyn in a neuronal cell line. We performed a genome-wide loss-of-function screen and a series of targeted screens in both cell lines to map the regulatory networks controlling endo-αSyn. The screen uncovered regulatory networks spanning many layers, from signaling, core transcription, RNA processing, translation, and protein posttranslational modifications, thus providing a rich dataset for future studies of αSyn regulation and function. Notably, we identified members of the decapping complex and Ubiquitin Fold Modifier (UFMylation) cascade as negative modulators of αSyn. As shown recently, the interaction of αSyn to the decapping components involves the first 20 amino acids (*36*). Thus, it will be interesting to further explore how NTA could regulate decapping module interactions and whether αSyn is a bona fide substrate of UFMylation.

We observed enzymes of the NatB complex to be the strongest negative regulators of endo-αSyn following *SNCA*, regardless of cell type. Loss of NTA, specifically by NatB, can affect many aspects of protein function, including stability, folding, and stress prevention (*38*, *53*). However, in our neuronal screens and follow-up experiments, depleting the NatB subunit NAA25 did not result in any obvious signs of toxicity, suggesting that NatB KD may be better tolerated in postmitotic cells than in dividing cells. This effect can be partially explained by previous observations in which less than 10% of NatB substrates completely lost acetylation in cells with moderate down-regulation of NatB enzymes. Our proteomics data agree with these results in which we observed fewer proteins than expected exhibiting differential expression in iNeurons lacking NAA25, supporting the idea that αSyn could be one of the few proteins sensitive to modest loss of NAA25. It remains unclear why αSyn is particularly susceptible to loss of NTA compared to other predicted NatB substrates. One possibility, supported by our work and others, is that intrinsically disordered proteins such as αSyn are stabilized by NTA, which is known to promote α-helicity of the N terminus of αSyn, thus promoting its binding to membranes where it may be stabilized by other binding partners.

N-terminal AcetylTransferases (NAT) inhibitors have been considered as potential anticancer drugs. NatB inhibition has been identified as a relevant therapeutic target for cancers such as hepatocellular carcinoma (*68*), prompting the development of small molecules that can inhibit its activity. While the undesirable effects associated with the general inhibition of NatB still need to be tested in vivo, a recent study highlighted the possibility of chemically targeting the interaction between αSyn and the NatB complex (*69*). Thus, our results will help generate interest and motivate future studies to develop inhibitors specifically targeting this interaction rather than a proteome-wide modification.

NatB constitutively acetylates αSyn in vivo. While NTA of αSyn has been shown to affect its stability (*45*), aggregation, and cellular toxicity (*44*), all these studies were performed using overexpressed and/or recombinant proteins. Here, we investigated the impact of removing this modification in a disease-relevant neuronal model. We observed a marked reduction in the stability of nonacetylated αSyn in three different cell lines, including iNeurons. We further showed that non–N-terminally acetylated αSyn is rapidly degraded by the proteasome, and the degradation of nonacetylated endo-αSyn was rescued in the absence of Ube2w in iNeurons also lacking NAA25, suggesting that the cross-talk between these modifications influences the stability of αSyn (Fig. 9).

αSyn predominantly exists in two different states: a highly unstructured cytosolic form and an α helix–mediated membrane-bound state (*60*). Understanding how lack of NTA affects the subcellular distribution of αSyn can shed light on its physiological role in the diseased and normal state. Our data provide evidence that lack of NTA specifically affects the cytosolic pool with little to no effect on the membrane-bound fraction (Fig. 9). Notably, we found that the membrane-bound fraction was composed mainly of the N-terminally acetylated species of αSyn. In addition, the lack of any substantial change in the membrane-bound fraction in the absence of NTA might be the consequence of rapid degradation of the cytosolic pool combined with the reduced off-rate of membrane-bound αSyn in intact cells. Membrane fractionation studies of αSyn from rat brains have demonstrated that αSyn shows very little dissociation from membranes once bound (*58*), suggesting that NTA αSyn may be stabilized on membranes by additional binding partners.

In this work, we found that METAP2 inhibition can efficiently lower αSyn levels in iNeurons that effectively model *SNCA* copy number variation found in patients with PD. While our data strongly demonstrate that down-regulation of METAP2 could serve as an appropriate therapy for synucleinopathies, a thorough evaluation of the drug's off-target effects, especially given the wide impact of NatB on the proteome, will be required to reinforce this hypothesis. In summary, our work provides a rich dataset of αSyn regulators for increased understanding of αSyn biology and will help devise more potent PD-specific therapeutic interventions. Furthermore, our experiments bring clarity to the subcellular distribution and degradation of αSyn in the absence of NTA.

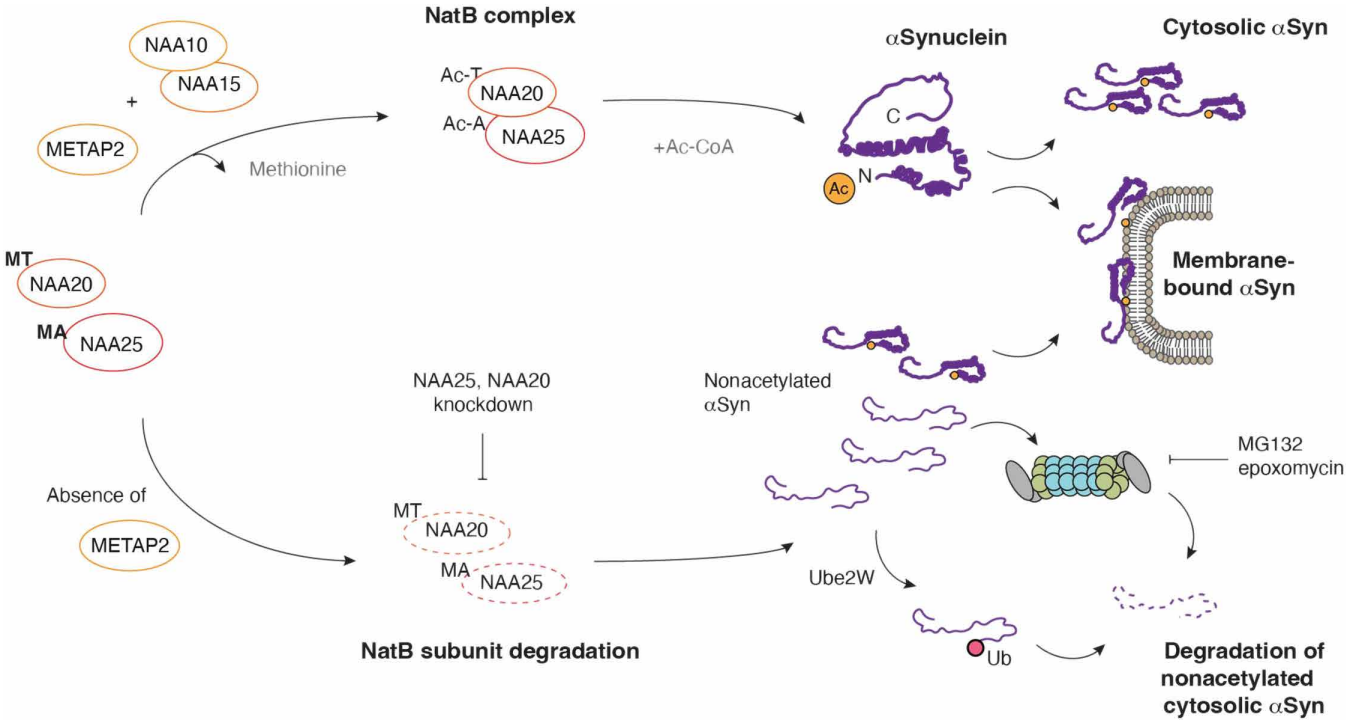

Fig. 9. Proposed mechanism illustrating the impact of loss of METAP2 and NAA25 on αSyn stability.

MATERIALS AND METHODS

Human cell lines

Human melanoma cell lines SKMEL30 (obtained from Memorial Sloan Kettering Cancer Center, SK1980-526) were maintained in RPMI 1640 medium (Gibco #11875085), supplemented with 10% (v/v) fetal bovine serum (FBS), 1 mM nonessential amino acids (NEAA; Gibco #11140-050), 1 mM sodium pyruvate (Gibco #11360-070), and penicillin/streptomycin (100 μg/ml; Gibco #15140-122). HEK293T cells (American Type Culture Collection, CRL-3216) were cultured in Dulbecco's modified Eagle's medium (DMEM; Gibco #11995-065) with 10% (v/v) FBS and 1 mM NEAA. The cells were grown at 37°C with 5% CO_2 to maintain physiological pH and were frequently tested for mycoplasma contamination.

Human iPSCs

Human CRISPRi-iPSCs (male WTC11 background) were seeded onto hESC-qualified Matrigel (Corning, #354277)–coated cell culture dishes and maintained in mTESR1 (STEMCELL Technologies, # 05850) medium. When 80 to 90% confluent, CRISPRi-iPSCs were dissociated using Versene (Gibco #15040-066) and split at a 1:6 ratio every 4 to 5 days onto Matrigel-coated dishes at the desired density in mTESR1 supplemented with 10 nM Y-27632 dihydrochloride ROCK inhibitor (Tocris #125410). PD patient–derived iPSCs carrying the *SNCA* triplication (4C) along with the piggyBac Ngn2 cassette and the mutation-corrected isogenic control iPSC lines (2C) with Ngn2 were a gift from V.K. (Brigham and Women's Hospital), and the generation of these lines is described in detail in the Supplementary Materials.

Human iNeurons

All the iPSC lines used in the study express doxycycline-inducible Ngn2 and were used to generate homogeneous iPSC-derived glutamatergic neurons using a previously described protocol (*25*). iPSCs were singularized using StemPro Accutase Cell Dissociation Reagent (Gibco #A11105-01), neutralized with mTESR1 media, centrifuged, and pelleted at 200*g* for 5 min. The pelleted cells were resuspended in induction media [IM recipe: KO DMEM/F12 (Gibco #12660-012), 1× NEAA, 1× N2 supplement (N2; Gibco #17502-048), NT-3 (10 ng/ml; PeproTech #450-03), brain-derived neurotrophic factor (BDNF) (10 ng/ml; PeproTech #450-02), mouse laminin (1 μg/ml; Thermo Fisher Scientific #23017-015), 10 nM Y27632 (ROCK inhibitor; Tocris #125410), and doxycycline hydrochloride (2 μg/ml; Sigma-Aldrich #D9891)], counted, and 7×10^5 cells were plated onto a Matrigel-coated well of a six-well plate in 2 ml of IM or 4.5×10^6 cells onto a 10-cm dish. Medium was changed every day with fresh supplements.

Three days after doxycycline induction, the cells were released with StemPro Accutase, centrifuged, pelleted, and resuspended in maturation media [MM recipe: half DMEM/F12 and half Neurobasal-A (Gibco #10888-022), 1× NEAA, 0.5× GlutaMAX (Gibco #35050-061), 0.5× N2, 0.5× B27 supplement (Gibco #17504-044), NT-3 (10 ng/ml), BDNF (10 ng/ml), mouse laminin (1μg/ml), 10 nM Y27632, and doxycycline hydrochloride (2 μg/ml)], counted, and 5×10^5 cells were plated onto freshly prepared poly-L-ornithine/laminin–coated wells of a 12-well culture dish or 11.5×10^6 cells onto a 15-cm dish. Some iPSC lines with individual gene KDs exhibited KD-related differences in the growth and survival of iPSCs/iNeurons. The same number of cells were plated for these iPSC cell lines during replating to avoid any density-related differences in differentiation or αSyn expression. The cells that were replated after 3 days of induction were termed "day 0 iNeurons." Half of the media was removed and replaced with new MM media with fresh supplements (minus doxycycline) on day 7. All media changes were made without doxycycline after day 7. All media changes were made without

doxycycline and Y27632 after day 7. Half of the media was removed and replaced with new MM media with fresh supplements (minus doxycycline and Y27632) on days 7 and 14. One-third of the media was removed and replaced with twice that volume with fresh supplements on day 21. One-third of the media was removed and replaced with the same volume of media on day 28.

Plasmids

To generate the EF1a-mNG21-10-2A-tdTomato vector, a gene block encoding mNG21-10 (IDT Technologies), a self-cleaving 2A peptide sequence, and a tdTomato fragment were PCR-amplified from the backbone pQC-NLS-tdTomato IX (Addgene plasmid #37347) and were inserted downstream of the EF1a promoter into the Eco RI– and Bsi WI–digested lenti-dCas9-VP64-Blast (Addgene plasmid #61425) backbone, thus replacing dCas9-VP64_Blast via three-piece Gibson assembly.

The donor plasmid for tagging the *SNCA* gene in CRISPRi-iPSCs was generated as follows: The 1-kb homology arms matching the 5′ and 3′ ends of the desired insertion site in the *SNCA* locus were PCR-amplified from genomic DNA. The homology arms were inserted into Nhe I/Bsr GI– and Kf lI/Mfe I–digested backbone AICS-DP-45: TTN-mEGFP (Addgene plasmid #114412) via a two-step two-piece Gibson assembly, thus replacing the human TTN gene homology arms in the construct with SNCA gene homology arms.

For the αSyn variant generation, αSyn was PCR-amplified from the plasmid pSIN-hSNCA-NE (Addgene plasmid #102366) with primers containing the desired mutations and was cloned into the FUW vector (Addgene plasmid #14882) or FUGW vector (Addgene plasmid #14883) digested using Xba I and Bam HI enzymes via a two-piece Gibson assembly. These constructs were generated with either a C-terminal NE tag or a C-terminal EGFP tag.

sgRNA target sequences for CRISPR-KO and KD were phosphorylated and annealed into oligo duplex and inserted into Bsm BI–digested lentiGuide-Puro (Addgene plasmid #52963), CROP-seq_puro (Addgene plasmid # 86708), or lenti-sgRNA Blast plasmids (Addgene plasmid #104993), respectively, using previously described protocols (*70*).

Lentiviral generation

Lentivirus was made for individual guides and plasmids by cotransfecting HEK293T cells with 1.06 μg of pMDLG (Addgene plasmid #12251), 0.57 μg of pMD2.G (Addgene plasmid #12259), 0.4 μg of pRSV-Rev (Addgene plasmid #12253) plasmid, and 1.6 μg of the lentiviral transfer plasmid, using a 1:3 ratio of total DNA to polyethylenimine (PEI) per well of a six-well plate. Lentiviruses for the pooled libraries were appropriately scaled based on the library size and were generated by cotransfecting 20×10^6 HEK293Ts seeded on a 0.1% gelatin–coated 15-cm dish with 13.25 μg of pMDLG, 7.2 μg of pMD2.G, 5 μg of pRSV-Rev, and 20 μg of pooled plasmid library using 136 μl of PEI. The medium was replaced the next day (DMEM +10% FBS or mTESR1), the supernatant was collected after 48 hours, passed through a 0.45 μM polyether sulfone filter to remove any cell debris, and the lentiviral aliquots were stored at −80°C, to be freeze-thawed only once.

SKMEL30 *SNCA*-tagged cell line generation

To generate the *SNCA*-tagged SKMEL30 cell line, we first generated SKMEL30 cells stably expressing the first 10 β strands of the Neongreen2 fluorescent protein, $mNG2_{1–10}$, by infecting the cells with the $mNG2_{1–10}$-2a-tdTomato lentivirus. Polyclonal cells positive for tdTomato were sorted on a FACSAria II (BD Biosciences) flow cytometer and termed "SKMEL30-$mNG2_{1–10}$" cells. Endogenous tagging of *SNCA* in SKMEL30-$mNG2_{1–10}$ was performed as previously described using Cas9/sgRNAs ribonucleoprotein complexes (RNPs) that were electroporated into the cells (*71*). Briefly, the reagents required for the assembly of RNPs—crRNA and tracrRNA oligos, 61 μM Cas9 protein (IDT Technologies, 1074182), and 200-nucleotide single-stranded DNA repair template designed with homologous flanking sequences around the *SNCA* C terminus—were purchased from IDT Technologies. For the assembly of RNPs, crRNA and tracrRNA oligos were incubated at 95°C for 5 min at a 1:1 molar ratio to generate duplexes. The duplex (130 pmol) was mixed with 100 pmol of Cas9 protein to make RNPs by incubating them at room temperature for 15 min. Before electroporation, the Cas9/sgRNA RNP complex was combined with 1 μl of the 100 mM single-stranded HDR template in a total volume of 5 μl of Neon buffer R. For the knock-in of $mNG2_{11}$, SKMEL30-$mNG2_{1–10}$ cells were mixed with the RNP/template mixture and were immediately electroporated with one pulse at 1650 V for 20 ms using the Neon Transfection system (Thermo Fisher Scientific).

Electroporated cells were cultured for at least 5 days before FACS analysis. mNG2-positive cells were isolated and expanded to make a polyclonal tagged cell population. Multiple single-cell clones were generated via single-cell sorting, and the $mNG2_{11}$ integration at the C terminus of *SNCA* was confirmed using genomic DNA PCR amplification. The selected bi-allelic clone, termed "$SKMEL30^{SNCA\text{-}mNG2}$," was further validated using Western blot and Sanger sequencing.

SNCA-tagged CRISPRi-iPSC cell line generation

For the endogenous tagging of *SNCA* in CRISPRi-iPSCs, we followed a previously described protocol (*26*) to tag genes that are not expressed in iPSCs. Briefly, crRNA oligos were designed to target the C terminus of the *SNCA* locus and were mixed with equimolar concentrations of tracrRNA and heated at 95°C for 5 min, cooled, and incubated at room temperature for a minimum of 15 min. RNPs were assembled by mixing duplexed crRNA:tracrRNA with 2 μg of Cas9 protein and then incubated at room temperature for 15 min to allow for complex formation.

iPSCs were harvested using Accutase, pelleted, and counted, and 8×10^5 cells were resuspended in 100 μl of Neon Buffer R with the RNP complex and 1 μg of the donor plasmid. The cells were electroporated with one pulse at 1300 V for 30 ms using the Neon Transfection system. Transfected cells were cultured on GFR Matrigel–coated (Corning #354230) six-well plates in mTESR1 with 10 nM ROCK inhibitor until the cells formed 10-cell colonies and expanded for 5 to 7 days for depleting the expression of mCherry from the donor plasmid. Following HDR, cells were harvested for FACS to isolate mCherry-positive cells. Forward scatter and side scatter (area versus width) were used to isolate live cells and doublets, and the mCherry-positive gate was drawn using live, no HDR donor control iPSCs. The polyclonal mCherry-positive iPSCs were transfected using similar conditions with mock or Tia1L-targeting RNP complexes. Cells were sorted 5 to 7 days after transfection for mCherry-negative cells mCherry-negative gate was drawn using live, mock RNP-transfected iPSCs), recovered, and clonal cell lines were generated using serial dilution. Integration of eGFP at the C terminus was confirmed using PCR using primers flanking and within the insertion site. The clones with the correct expected size

PCR amplicons were further validated using sequencing to verify the in-frame insertion of eGFP.

Primary genome-wide screen in SKMEL30$^{SNCA\text{-}mNG2}$

The lentiCas9-Blast construct (Addgene plasmid #52962) was used to express Cas9 in SKMEL30$^{SNCA\text{-}mNG2}$ cell lines. One million SKMEL30$^{SNCA\text{-}mNG2}$ cells were transduced with 100 μl of the lentiCas9-Blast lentivirus in media containing Polybrene (10 μg/ml). The polyclonal Cas9-expressing SKMEL30$^{SNCA\text{-}mNG2}$ cells were generated after applying selection pressure using blasticidin (5 μg/ml; Thermo Fisher Scientific #A1113903) for 5 days.

Genome-wide plasmid library preparation

The genome-wide human sgRNA Brunello library with an average of 4 sgRNAs per gene and 1000 NTC guides was purchased from Addgene (#73178). The library was transformed into electrocompetent cells (Lucigen #60242-1) using a gene pulser (Bio-Rad) and recovered for 16 to 18 hours at 32°C to prevent recombination. The plasmid DNA was prepared (Endotoxin-free Plasmid Maxiprep kit, Qiagen) from the cells and was sequenced to confirm the library distribution and representation.

Lentivirus titering in SKMEL30

Virus volume needed to achieve low multiplicity of infection (MOI) in SKMEL30$^{SNCA\text{-}mNG2}$ was determined as follows: 2×10^6 cells were plated per well of a 12-well plate with different virus volumes. The medium was supplemented with Polybrene (8 μg/ml) to improve transduction efficiency. After 24 hours, the cells were split into duplicate wells, one of which was treated with puromycin (1 μg/ml). Cells were selected for 3 days, lifted, and counted. The percent transduction (cell count with puromycin/cell count without puromycin multiplied by 100) was calculated, and the virus volume with approximately 30% cell survival was chosen for the genome-wide screening.

FACS-based CRISPR-KO screen for αSyn levels

Cas9 SKMEL30$^{SNCA\text{-}mNG2}$ cells were infected with the Brunello lentiviral library at a low MOI in a 12-well format with Polybrene (8 μg/ml). One day after infection, the cells were moved to 15-cm dishes and were expanded for an additional 2 days before puromycin selection (1 μg/ml). After selection and expansion, a fraction of the cells was harvested on day 8 for genomic DNA extraction. The remaining cells were cultured without puromycin for an additional week. For the CRISPR-KO screen, cells were lifted on day 15 following transduction, resuspended in a sorting buffer (1× PBS, 2% FBS, and 1 mM EDTA), and were FACS-sorted using an 85-μm nozzle. The cells with the highest 20% and lowest 20% αSyn expression levels were sorted on the basis of the mNG2/tdTomato ratio (gated from the live, single, and tdTomato-positive population) signal distribution. The sorted cells were pelleted and frozen for downstream analysis.

DNA extraction, PCR amplification, and NGS

Thawed cell pellets were resuspended in lysis buffer [50 mM tris, 50 mM EDTA, and 1% SDS (pH 8)] to release cell components. Proteinase K (Qiagen #19131) was added just before use to remove protein contaminants, and the sample was incubated at 55°C overnight. Following overnight incubation, ribonuclease A (10 mg/ml; Qiagen #19101) was added to the lysed sample. The sample was mixed thoroughly and incubated at 37°C for 30 min before placing in ice. Prechilled 7.5 M ammonium acetate was added to the cooled samples to precipitate proteins. The samples were vortexed and spun at >4000*g* for 10 min. The supernatant was withdrawn, and the DNA was precipitated with 100% isopropanol. The genomic DNA was further purified using 70% ethanol, and the sample was spun at high speed to pellet the DNA. The genomic DNA pellet was air-dried and resuspended in TE buffer, and the DNA was quantified using Nanodrop.

PCR amplification was performed using custom primers containing necessary Illumina adaptors and barcodes for multiplexing different samples from the screen. The primers also specifically amplify genome-integrated parts of the lentiGuide-puro (Addgene #52963) backbone. PCR reactions were performed in a volume of 100-μl reactions containing 5 μg of gDNA, 0.5 μM of each primer (forward and reverse), 2.5 mM of deoxynucleotide triphosphates, 1× Takara ExTaq buffer (10×), and 0.5 μl of the enzyme (Takara #RR001A). The resulting PCR products were gel-extracted, quantified using Qubit dsDNA HS Assay (Thermo Fisher Scientific #Q32851), pooled together in equimolar ratios, and sequenced using a Nextseq 500/550 v2 75 cycle kit (Illumina #20024906). Amplifications were carried out with 1 × 8 cycles for sample index reads and 1 × 63 cycles for the sgRNA.

Secondary screen in SKMEL30$^{SNCA\text{-}mNG2}$

The secondary screen pooled library contained 992 sgRNAs targeting the top positive and negative regulators of αSyn based on a 5% FDR cutoff in the primary screen, essential gene sgRNAs, and 2000 NTC sgRNAs. A pool of sgRNAs containing oligonucleotides was ordered as a pool of equimolar oligos from Twist Biosciences with Bsm BI–compatible overhangs, PCR-amplified, and cloned into Bsm BI–digested lentiGuide-puro backbone. Library virus generation and titration were performed as previously described. Twenty-five million SKMEL30$^{SNCA\text{-}mNG2}$ cells were transduced with the focused secondary library, appropriately scaled down based on the library size, selected with puromycin, and sorted 14 days after transduction corresponding to the highest 20% and lowest 20% αSyn expression levels using both the mNG2/tdTomato and mNG2/4′,6-diamidino-2-phenylindole (autofluorescence) ratios to identify false positives. Processing of the screen samples and sequencing by NGS were performed as previously described.

Secondary screen in *SNCA*-tagged iNeurons

The CRISPRi sublibrary contained 3460 sgRNAs targeting the top 100 positive and negative regulators of αSyn identified in the SKMEL30 screen, with an average of 10 sgRNAs per gene selected from the genome-wide CRISPRi library hCRISPRi-v2 (*27*), and 992 NTC sgRNAs. The custom library was ordered as a pool of oligonucleotides from Twist Biosciences with Bsm BI–compatible overhangs, PCR-amplified, and cloned into Bsm BI–digested CROPseq-puro-v2 backbone (Addgene #127458). The generated CRISPRi library was packaged into lentivirus as described previously. *SNCA*-tagged CRISPRi-iPSCs were singularized using accutase and seeded at a density of ~60,000 cells/cm^2 onto Matrigel-coated 10-cm dishes in mTESR1 medium supplemented with 10 nM ROCK inhibitor and the lentiviral sgRNA library. Twenty four hours after transduction, the culture medium was carefully replaced with mTESR1 supplemented with 10 nM ROCK inhibitor. The following day, the cells were lifted and replated onto Matrigel-coated 15-cm dishes at a

density of ~50,000 cells/cm^2 in mTESR1 media supplemented with 10 nM ROCK inhibitor and puromycin (0.5 μg/ml). Two days later, puromycin concentration was increased to 1 μg/ml without ROCK inhibitor. The initial MOI, as measured by the number of cells that survived puromycin selection, was between 10 and 15%. Following selection pressure, one-third of the cells were harvested for neuronal differentiation, and the remaining fractions were frozen and were used as an "iPSC time-point" for NGS.

SNCA-tagged CRISPRi-iPSCs, transduced with the sublibrary, were seeded onto Matrigel-coated 10-cm dishes at a density of ~80,000 cells/cm^2 and at a 5000× coverage for neuronal differentiation. The iPSCs were maintained in "induction media" for 3 days and were replated onto Poly-L-Ornithine/laminin-coated 15-cm dishes at the same density of ~80,000 cells/cm^2 but at a 10,000× coverage per guides present in the sublibrary. A fraction of the iNeurons was harvested as the "neuronal time point" for NGS. Day 14 and day 28 iNeurons, counted from the day of replating, were released using papain as previously described and sorted into the top 25% and the bottom 25% of the GFP-positive population gated on the basis of the fluorescein isothiocyanate-A signal distribution. The estimated library coverage of the sorted population from both the time points was roughly between 150× and 200× coverage per library element. Genomic DNA was extracted with the QIAamp DNA Micro Kit (Qiagen# 56304), and the DNA was quantified using Nanodrop. PCR amplification and sample preparation were performed as previously described and sequenced using a Nextseq 1000/2000 v3 100 cycle kit (Illumina# 20046811). Amplifications were carried out with 1 × 8 cycles for sample index reads and 1 × 92 cycles for the sgRNA.

Dissociation and FACS sorting of iNeurons

For harvesting the iNeurons for flow cytometry, we followed a previously described protocol (*25*). Briefly, iNeurons derived from *SNCA*-tagged CRISPRi-iPSCs were harvested at various time points using papain solution (20 U/ml; Worthington; PAP2# LK003178) supplemented with 5 mM magnesium chloride and deoxyribonuclease (DNase) (5 μg/ml; Worthington; D2# LK003172). One hundred units of papain per vial was reconstituted with 5 ml of Hanks' balanced salt solution and activated by placing the solution at 37°C for 10 min. The activated papain, along with magnesium chloride and DNase, was added to the iNeurons, at 250 μl per well of a 12-well plate or 7.5 ml per 15-cm dish and incubated at 37°C for 10 min. The papain solution was neutralized using DMEM plus 10% FBS, and the cells were gently triturated, collected in an Eppendorf tube, and spun at 200*g* for 10 min. The pellet was resuspended (5 million cells/ml) in FACS resuspension buffer [1× PBS + 2 mM EDTA + 2% bovine serum albumin (BSA) + 25 mM Hepes], passed through a 35-μm cell strainer cap, and was sorted/analyzed on the BD FACS Aria Fusion using the 85 μM nozzle. The collection tubes were coated with 1× PBS + 20% BSA solution, and the sorted iNeurons were collected in the same solution.

Generation of single/double sgRNA KD cells

For validation by CRISPRi KD in iNeurons, CRISPRi- and *SNCA*-tagged CRISPRi-iPSCs were transduced with two to seven guides selected per gene at high MOI. Transduced cells were selected either for 5 days with blasticidin (4 μg/ml) or for 3 to 4 days with puromycin (1 μg/ml), expanded for 3 to 4 days, and differentiated to iNeurons as described above. The iNeurons were harvested at the desired time points for biochemistry [Western blot and enzyme-linked immunosorbent assay (ELISA)], FACS analysis, and proteomics.

Validation using small-molecule inhibitors

For validation using small-molecule inhibitors in iNeurons, *SNCA*-tagged CRISPRi-iPSCs were differentiated to iNeurons. Day 7 iNeurons were treated with the drugs, TNP470 (Cayman Chemical #16449) or GSK-LSD1 (Tocris #5361) dissolved in dimethyl sulfoxide (DMSO), or DMSO only (control) at different desired concentrations. The iNeurons were harvested using papain for FACS analysis on days 14 and 20. All experiments were performed in duplicate.

Immunocytochemistry

SKMEL30$^{SNCA\text{-}mNG2}$ cells were grown on standard glass coverslips and were fixed with 4% formaldehyde at room temperature for 10 min, washed with 1× PBS three times, and mounted onto slides using Prolong Glass Antifade Mountant with NucBlue stain (Thermo Fisher Scientific #P36981). Images were acquired using a Leica SP8 confocal 63× immersion oil objective. iNeurons derived from *SNCA*-tagged CRISPRi-iPSCs were fixed at different time points directly in the culture media using 8% (w/v) paraformaldehyde (diluted in PBS) at room temperature for 20 min. The cells were then washed with 1× PBS three times, permeabilized with 0.1% Triton X-100 at room temperature for 30 min, and stained with rabbit anti–β3-tubulin antibody (1:1000; Abcam #ab18207) and chicken anti-MAP2 antibody (1:5000; Abcam #ab5392) overnight at 4°C. The following day, the cells were washed three times with 1×PBS and then incubated with secondary antibodies for 2 hours at room temperature, washed with 1× PBS three times, and mounted onto slides using Prolong Glass Antifade Mountant with NucBlue stain (Thermo Fisher Scientific #P36981). Images were acquired using a Ti-E Eclipse inverted epifluorescence microscope (Nikon) with a 40× immersion oil objective.

Western blotting

Protein lysates were prepared by lysing cells directly on the tissue culture dishes using radioimmunoprecipitation assay (RIPA) buffer supplemented with 1× protease inhibitor cocktail (Sigma-Aldrich). Lysates were centrifuged at 13,000*g* for 10 min at 4°C, and the supernatant was carefully transferred to fresh tubes. Protein concentration of the lysates was quantified using bicinchoninic acid protein assay, and 15 to 20 μg of protein from each sample was loaded for electrophoresis onto 4 to 20% mini-protean protein gels (Bio-Rad #4561096) and transferred to a polyvinylidene difluoride membrane (Millipore) for 60 min at 100 V at 4°C according to standard protocols. The membranes following transfer were treated with 4% paraformaldehyde diluted in PBS for 30 min at room temperature to improve the detection of endo-αSyn as previously described (*72*). The blot was rinsed three times with tris-buffered saline (TBS) plus 0.1% Tween-20 (TBST) and blocked using 1× TBST with 1% casein for 30 min at room temperature. Membranes were incubated with the primary antibodies at 4°C overnight, washed three times with TBST, and then incubated with secondary antibodies at room temperature for 2 hours. The membranes were then washed three times with TBST and imaged on an Odyssey Fc imaging system (LI-COR), and the images were processed using Image Studio software. Primary antibodies used were mouse anti-αSyn (1:20,000; 9027, a gift from K.L.), mouse anti-αSyn (1:1000; BD Biosciences #510786),

rabbit anti-αSyn (1:1000; Millipore #40-1053), mouse anti-SNAP25 (1:1000; BioLegend #836304), rabbit anti–glyceraldehyde-3-phosphate dehydrogenase (GAPDH) (1:10,000; Cell Signaling Technology #2118S), mouse anti-Tuj1(1:5000; BioLegend #801213), mouse anti-VDAC1 (1:1000; Millipore #MABN504), rabbit anti-NAA20 (Thermo Fisher Scientific #PA5-112622), rabbit anti-NAA25 (Thermo Fisher Scientific #PA5-98409), and mouse anti–α-tubulin (Novus Biologicals #NB100-690). Secondary antibodies used were IRDye 680RD goat anti-mouse immunoglobulin G (IgG) (1:10,000; LI-COR #926-6807) and IRDye 800CW goat anti-rabbit IgG (1:10,000; LI-COR #926-32211).

Proteomics and ELISA

These are described in detail in the Supplementary Materials.

Expression of acetylated and nonacetylated αSyn in mammalian cells

Endo-αSyn was knocked down by CRISPRi, and iPSCs were differentiated to iNeurons. Upon replating, iNeurons were transduced at equal MOI with either FUW-SNCA^{WT}, FUW-SNCA^{D2R} (mixed NTA mutant), or FUW-SNCA^{D2E} (positive control) and harvested 14 days later in RIPA lysis buffer for anti-αSyn (BD Biosciences, 510786) immunoblot. $N = 3$ independent transductions were performed for each sample group at each titer. HEK293T cells were transduced with lentivirus containing either pSIN-hSNCA-NE^{WT} (Addgene #102366), pSIN-SNCA-NE^{D2R}, pSIN-SNCA-NE^{D2Y}, or empty lentivirus (control) at equal MOI as determined by lentiviral titer. Lentiviruses were produced, titered, and transduced in parallel. Cells were harvested 96 hours after transduction in RIPA lysis buffer, and αSyn levels were measured by anti-αSyn (BD Biosciences #510786) immunoblot. $N = 3$ independent transductions were performed for each sample group at each titer.

αSyn turnover

Chx chase was performed in HEK293T cells, as previously described (*73*), with slight modification. One hundred twenty hours after transduction of either αSyn^{WT} or αSyn^{D2R}, HEK293T cells were treated with Chx (25 μg/ml; Sigma-Aldrich) and harvested in RIPA lysis buffer at the indicated time points for analysis by anti-αSyn immunoblot. $N = 3$ independent transductions and Chx treatments were performed for each sample group at each indicated time point.

Calculation of αSyn acetylation levels

pSIN-SNCA-NE^{WT} and pSIN-SNCA-NE^{D2R} were transfected into HEK293T cells supplemented with leupeptin and pepstatin (10 μg/ml), each, and harvested 48 hours later for immunoprecipitation (IP), essentially as previously described (*73*). Briefly, the cell lysate was centrifuged for 10 min at 17,000*g* at 4°C, and then the supernatant was divided equally into two tubes (IP and no IgG control). Five percent of the total lysate was kept for the total input lane. The lysate was incubated with anti-αSyn antibody (IP) or no antibody (no IgG control), rotating at 4°C for 4 hours, followed by an additional 2 hours with Protein-G Magnetic Sepharose (Cytiva #28944008). The Sepharose was washed three times, and the protein was eluted into 125 mM tris (pH 8.0) supplemented with 4% sodium dodecyl sulfate (w/v) and 10 mM 1,4-dithiothreitol. Acetylation of immunoprecipitated αSyn^{WT} or αSyn^{D2R} and recombinant nonacetylated αSyn or N-terminally acetylated αSyn was confirmed by a ~42-Da mass shift by MALDI-TOF MS on a Brüker Rapiflex [funding source: National Institutes of Health (NIH) 1S10OD030460-01], using protein standard calibration 1 (4 to 20 kDa). Immunoprecipitated and recombinant proteins were diluted 100-fold in 70/30 acetonitrile supplemented with 0.1% trifluoroacetic acid to dilute the detergent and spotted on 2,5-dihydroxybenzoic acid matrix. Predicted masses are as follows: Immunoprecipitated αSyn-NE^{WT}: nonacetylated (16,584.23 Da); acetylated (16,626.23 Da). Immunoprecipitated αSyn-NE^{D2R}: nonacetylated (16,625.33 Da); acetylated (16,667.33 Da). Recombinant αSyn: nonacetylated (14,460.16 Da); acetylated (14,502.16 Da). We did not detect any Met-cleaved αSyn-NE^{D2R} protein (expected at 16,476.12 Da).

The percentage of acetylated αSyn-NE^{D2R} was determined by calculating a MALDI standard curve using ratios of the peak signal intensities for nonacetylated (~14,460 Da) and acetylated (~14,502 Da) recombinant αSyn. The ratios were determined using mixtures of known concentrations of nonacetylated to acetylated recombinant αSyn proteins (0, 10, 25, 50, 75, 90, and 100% acetylated αSyn). Three independent MS spectra were obtained for each mixture, and the percentage of acetylated αSyn was calculated for αSyn-NE^{WT} ($n = 3$ independent IPs) and αSyn-NE^{D2R} ($n = 5$ independent IPs).

αSyn purification from Escherichia coli

N-terminally acetylated and nonacetylated αSyn were expressed in either BL21(DE3) cells expressing NatB complex components or BL21(DE3) cells, respectively, as previously described (*42*). Briefly, αSyn was cloned into the pTXB1 vector with a C-terminal intein-6xHis fusion. Protein was expressed in BL21(DE3) with 1 mM isopropyl-β-D-1-thiogalactopyranoside at 18°C, shaken overnight for 16 hours. Following pelleting of bacteria (4000*g* for 20 min at 4°C) and resuspension in lysis buffer [20 mM tris (pH 8.3), 1 Roche protease inhibitor tablet, lysozyme (1 mg/ml), and 20 mM imidazole], cells were sonicated on ice (2 min; 1-s on, 2-s off) and centrifuged again (20,000 *g*, 30 min at 4°C). αSyn-intein-6xHis was affinity-captured from the supernatant using Ni-NTA resin (Thermo Fisher Scientific #PI88222) followed by elution with 25 mM tris (pH 8.3) buffer supplemented with 300 mM imidazole. Intein cleavage was carried out by the addition of 200 mM β-mercaptoethanol (β-ME) with agitation at room temperature overnight (16 hours). The full-length αSyn was dialyzed into 20 mM tris (pH 8.3) to remove the β-ME and imidazole, and a reverse-Ni column was performed to remove the cleaved intein-6xHis. Last, αSyn was purified by ion-exchange chromatography into 20 mM tris (pH 8.3) on a NaCl gradient. αSyn was eluted at ~300 mM NaCl. The eluted protein was pooled and loaded onto an S200 size exclusion column in 25 mM tris (pH 8), 100 mM NaCl, 1 mM EDTA, and 0.5 mM tris(2-carboxyethyl)phosphine (TCEP). The purity of the final fractions was assessed by SDS–polyacrylamide gel electrophoresis (SDS-PAGE) gel followed by Coomassie blue stain, and only the pure fractions were combined, concentrated, and flash-frozen as small aliquots for storage at −80°C.

Subcellular cytosol-membrane fractionation

Cytosol-membrane fractions were separated from transfected HEK293T cells and transduced iNeurons as previously described (*73*). In these experiments: For HEK293T cultures, cells were transfected with either pSIN-SNCA-NE^{WT} or pSIN-SNCA-NE^{D2R} for 72 hours. $N = 3$ independent cultures and transfections per sample group. For measurement of αSyn mutants in induced neuron (iN) cultures, iPSCs stably expressing dCAS9-KRAB were first transduced

with an sgRNA against *SNCA*. Following blasticidin selection, iNeurons were induced and transduced with either UbC-SNCA^{WT}, UbC-SNCA^{D2R}, or UbC-SNCA^{D2E} and aged for 28 days. $N = 4$ independent cultures per sample group. To measure endo-αSyn in iNeurons, iPSCs stably expressing dCAS9-KRAB were transduced with sgRNAs for either NTC or NAA25. NAA25 CRISPRi-mediated KD was too efficient at depleting endogenous synuclein levels for us to measure endogenous synuclein distribution. Therefore, we performed low MOI CRISPRi KD to only modestly KD NAA25 levels for these measurements. Following puromycin selection, iNeurons were aged for 42 days. $N = 3$ independent cultures per sample group. All cells were harvested in 1× PBS supplemented with protease and phosphatase inhibitors (no detergent) and mechanically lysed with a syringe, followed by ultracentrifugation at 300,000*g* for 1 hour at 4°C to separate cytosolic and membrane fractions. The pellet (membrane fraction) was resuspended in an equal volume of lysis buffer as the supernatant (cytosol fraction). Both fractions were supplemented with 1% SDS final (v/v), sonicated, and boiled for 20 min at 95°C. Equivalent volumes of each fraction were loaded onto SDS-PAGE, followed by anti-αSyn immunoblot.

Measurement of acetylated and nonacetylated membrane-bound αSyn

HEK293T cells were transfected with pSIN-SNCA-NE^{WT} or pSIN-SNCA-NE^{D2R} and harvested 72 hours after transfection, as described in the "Subcellular cytosol-membrane fractionation" section. Following subcellular fractionation of cytosol and membrane proteins, the two fractions were supplemented with 1% SDS final (v/v) and rotated at 4°C for 30 min to release membrane-bound proteins. Debris was pelleted at 17,000*g* at 4°C for 10 min, and αSyn was immunoprecipitated from the supernatant for each fraction as described in the "Calculation of αSyn acetylation levels" section. Three independent transfections and independent IPs were pooled together and then subjected to MALDI-TOF to qualitatively measure nonacetylated and acetylated αSyn levels in the cytosolic and membrane-bound fractions. The counts were normalized to the maximum data point for the membrane fraction to allow for signal intensity comparison between non-NTA and NTA αSyn in each fraction.

Screen data analysis

Raw FASTQ files were processed to extract the sgRNA spacer sequence using the following regular expression "CCG[ACGT]{18,21}GTT." Spacer sequences were then mapped to the library using a Bowtie short read aligner with parameters -v 0 -m 1 to generate an sgRNA count matrix that can be loaded into the R programming environment. Raw sgRNA counts were normalized using the regularized log transformation as part of the DESeq2 package. Gene phenotype was calculated by taking the mean of the two sgRNAs with the absolute largest fold change. Gene *P* value was calculated by comparing the mean of all sgRNAs per gene to an empirically generated distribution of means generated by 500,000 permutations of the association between sgRNAs and genes in the data. NTCs were randomly divided into groups of four sgRNAs.

For the secondary CRISPRi screen in iNeurons, raw FASTQ files were processed to extract the sgRNA spacer sequence using the following regular expression CCG[ACGT]{18,21}GTT. Spacer sequences were then mapped to the library using a Bowtie short read aligner with parameters -v 0 -m 1 to generate an sgRNA count matrix that can be loaded into the R programming environment. In this screen, because of a very different distribution of values between the group of genes that had a negative effect on αSyn protein levels to the rest of the sgRNAs, we normalized the data using the function normalize.loess, which is part of the affy Bioconductor package, by passing to the argument "subset" the indices of only the NTC sgRNAs. Gene phenotypes were calculated as the mean of the three sgRNAs with the absolute largest fold change, and *P* values were calculated by comparing the mean of all sgRNAs per gene to an empirically generated distribution of means generated by 500,000 permutations of the association between sgRNAs and genes in the data using only the NTC sgRNAs.

Statistical analysis

Statistical analyses were performed using R (Rstudio Team, 2022), the tidyverse package (*74*), and Prism GraphPad 9.3.0 software (GraphPad Software, San Diego, CA). The significance of the difference was determined for majority of the analysis using a one-way analysis of variance (ANOVA) test, followed by Tukey's multiple comparison test when comparing more than two groups. A *P* value of 0.05 or less was considered significant. Specific statistical tests are indicated in the figure legends for each experiment.

Supplementary Materials

This PDF file includes:

Supplementary Text
Figs. S1 to S8
Legends for tables S1 to S5
References

Other Supplementary Material for this manuscript includes the following:

Tables S1 to S5

REFERENCES AND NOTES

1. A. B. Singleton, M. Farrer, J. Johnson, A. Singleton, S. Hague, J. Kachergus, M. Hulihan, T. Peuralinna, A. Dutra, R. Nussbaum, S. Lincoln, A. Crawley, M. Hanson, D. Maraganore, C. Adler, M. R. Cookson, M. Muenter, M. Baptista, D. Miller, J. Blancato, J. Hardy, K. Gwinn-Hardy, α-Synuclein locus triplication causes Parkinson's disease. *Science* **302**, 841 (2003).
2. M.-C. Chartier-Harlin, J. Kachergus, C. Roumier, V. Mouroux, X. Douay, S. Lincoln, C. Levecque, L. Larvor, J. Andrieux, M. Hulihan, N. Waucquier, L. Defebvre, P. Amouyel, M. Farrer, A. Destée, α-Synuclein locus duplication as a cause of familial Parkinson's disease. *Lancet* **364**, 1167–1169 (2004).
3. P. Ibáñez, A.-M. Bonnet, B. Débarges, E. Lohmann, F. Tison, P. Pollak, Y. Agid, A. Dürr, A. Brice, Causal relation between α-synuclein locus duplication as a cause of familial Parkinson's disease. *Lancet* **364**, 1169–1171 (2004).
4. F. Soldner, Y. Stelzer, C. S. Shivalila, B. J. Abraham, J. C. Latourelle, M. I. Barrasa, J. Goldmann, R. H. Myers, R. A. Young, R. Jaenisch, Parkinson-associated risk variant in distal enhancer of α-synuclein modulates target gene expression. *Nature* **533**, 95–99 (2016).
5. C. Blauwendraat, M. A. Nalls, A. B. Singleton, The genetic architecture of Parkinson's disease. *Lancet Neurol.* **19**, 170–178 (2020).
6. A. T. Rodger, M. ALNasser, W. G. Carter, Are therapies that target α-synuclein effective at halting Parkinson's disease progression? A systematic review. *Int. J. Mol. Sci.* **24**, (2023).
7. Y. C. Wong, D. Krainc, α-synuclein toxicity in neurodegeneration: Mechanism and therapeutic strategies. *Nat. Med.* **23**, 1–13 (2017).
8. P. Brundin, K. D. Dave, J. H. Kordower, Therapeutic approaches to target α-synuclein pathology. *Exp. Neurol.* **298**, 225–235 (2017).
9. S. Ltic, M. Perovic, A. Mladenovic, N. Raicevic, S. Ruzdijic, L. Rakic, S. Kanazir, α-Synuclein is expressed in different tissues during human fetal development. *J. Mol. Neurosci.* **22**, 199–204 (2004).
10. K. Taguchi, Y. Watanabe, A. Tsujimura, M. Tanaka, Expression of α-synuclein is regulated in a neuronal cell type-dependent manner. *Anat. Sci. Int.* **94**, 11–22 (2019).
11. M. W. C. Rousseaux, G. E. Vázquez-Vélez, I. Al-Ramahi, H.-H. Jeong, A. Bajić, J.-P. Revelli, H. Ye, E. T. Phan, J. M. Deger, A. M. Perez, J.-Y. Kim, L. A. Lavery, Q. Xu, M. Z. Li, H. Kang, J. J. Kim, J. M. Shulman, T. F. Westbrook, S. J. Elledge, Z. Liu, J. Botas, H. Y. Zoghbi,

A druggable genome screen identifies modifiers of α-synuclein levels via a tiered cross-species validation approach. *J. Neurosci.* **38**, 9286–9301 (2018).
12. M. W. Rousseaux, M. de Haro, C. A. Lasagna-Reeves, A. De Maio, J. Park, P. Jafar-Nejad, I. Al-Ramahi, A. Sharma, L. See, N. Lu, L. Vilanova-Velez, T. J. Klisch, T. F. Westbrook, J. C. Troncoso, J. Botas, H. Y. Zoghbi, TRIM28 regulates the nuclear accumulation and toxicity of both α-synuclein and tau. *eLife* **5**, e19809 (2016).
13. V. Khurana, J. Peng, C. Y. Chung, P. K. Auluck, S. Fanning, D. F. Tardiff, T. Bartels, M. Koeva, S. W. Eichhorn, H. Benyamini, Y. Lou, A. Nutter-Upham, V. Baru, Y. Freyzon, N. Tuncbag, M. Costanzo, B.-J. San Luis, D. C. Schöndorf, M. I. Barrasa, S. Ehsani, N. Sanjana, Q. Zhong, T. Gasser, D. P. Bartel, M. Vidal, M. Deleidi, C. Boone, E. Fraenkel, B. Berger, S. Lindquist, Genome-scale networks link neurodegenerative disease genes to α-synuclein through specific molecular pathways. *Cell Syst.* **4**, 157–170.e14 (2017).
14. S. Mittal, K. Bjørnevik, D. S. Im, A. Flierl, X. Dong, J. J. Locascio, K. M. Abo, E. Long, M. Jin, B. Xu, Y. K. Xiang, J.-C. Rochet, A. Engeland, P. Rizzu, P. Heutink, T. Bartels, D. J. Selkoe, B. J. Caldarone, M. A. Glicksman, V. Khurana, B. Schüle, D. S. Park, T. Riise, C. R. Scherzer, β2-Adrenoreceptor is a regulator of the α-synuclein gene driving risk of Parkinson's disease. *Science* **357**, 891–898 (2017).
15. J. R. Patterson, W. D. Hirst, J. W. Howe, C. P. Russell, A. Cole-Strauss, C. J. Kemp, M. F. Duffy, J. Lamp, A. Umstead, M. Kubik, A. C. Stoll, I. E. Vega, K. Steece-Collier, Y. Chen, A. C. Campbell, C. L. Nezich, K. E. Glajch, C. E. Sortwell, β2-adrenoreceptor agonist clenbuterol produces transient decreases in α-synuclein mRNA but no long-term reduction in protein. *NPJ Parkinsons Dis.* **8**, 61 (2022).
16. C. Pacini, J. M. Dempster, I. Boyle, E. Gonçalves, H. Najgebauer, E. Karakoc, D. van der Meer, A. Barthorpe, H. Lightfoot, P. Jaaks, J. M. McFarland, M. J. Garnett, A. Tsherniak, F. Iorio, Integrated cross-study datasets of genetic dependencies in cancer. *Nat. Commun.* **12**, 1661 (2021).
17. J. M. Dempster, C. Pacini, S. Pantel, F. M. Behan, T. Green, J. Krill-Burger, C. M. Beaver, S. T. Younger, V. Zhivich, H. Najgebauer, F. Allen, E. Gonçalves, R. Shepherd, J. G. Doench, K. Yusa, F. Vazquez, L. Parts, J. S. Boehm, T. R. Golub, W. C. Hahn, D. E. Root, M. J. Garnett, A. Tsherniak, F. Iorio, Agreement between two large pan-cancer CRISPR-Cas9 gene dependency data sets. *Nat. Commun.* **10**, 5817 (2019).
18. M. Uhlen, P. Oksvold, L. Fagerberg, E. Lundberg, K. Jonasson, M. Forsberg, M. Zwahlen, C. Kampf, K. Wester, S. Hober, H. Wernerus, L. Björling, F. Ponten, Towards a knowledge-based Human Protein Atlas. *Nat. Biotechnol.* **28**, 1248–1250 (2010).
19. J. H. Olsen, S. Friis, K. Frederiksen, Malignant melanoma and other types of cancer preceding Parkinson disease. *Epidemiology* **17**, 582–587 (2006).
20. S. Feng, S. Sekine, V. Pessino, H. Li, M. D. Leonetti, B. Huang, Improved split fluorescent proteins for endogenous protein labeling. *Nat. Commun.* **8**, 370 (2017).
21. J. G. Doench, N. Fusi, M. Sullender, M. Hegde, E. W. Vaimberg, K. F. Donovan, I. Smith, Z. Tothova, C. Wilen, R. Orchard, H. W. Virgin, J. Listgarten, D. E. Root, Optimized sgRNA design to maximize activity and minimize off-target effects of CRISPR-Cas9. *Nat. Biotechnol.* **34**, 184–191 (2016).
22. O. Shalem, N. E. Sanjana, E. Hartenian, X. Shi, D. A. Scott, T. Mikkelson, D. Heckl, B. L. Ebert, D. E. Root, J. G. Doench, F. Zhang, Genome-scale CRISPR-Cas9 knockout screening in human cells. *Science* **343**, 84–87 (2014).
23. K. R. Sanson, R. E. Hanna, M. Hegde, K. F. Donovan, C. Strand, M. E. Sullender, E. W. Vaimberg, A. Goodale, D. E. Root, F. Piccioni, J. G. Doench, Optimized libraries for CRISPR-Cas9 genetic screens with multiple modalities. *Nat. Commun.* **9**, 5416 (2018).
24. L. A. Gilbert, M. A. Horlbeck, B. Adamson, J. E. Villalta, Y. Chen, E. H. Whitehead, C. Guimaraes, B. Panning, H. L. Ploegh, M. C. Bassik, L. S. Qi, M. Kampmann, J. S. Weissman, Genome-scale CRISPR-mediated control of gene repression and activation. *Cell* **159**, 647–661 (2014).
25. R. Tian, M. A. Gachechiladze, C. H. Ludwig, M. T. Laurie, J. Y. Hong, D. Nathaniel, A. V. Prabhu, M. S. Fernandopulle, R. Patel, M. Abshari, M. E. Ward, M. Kampmann, CRISPR interference-based platform for multimodal genetic screens in human iPSC-derived neurons. *Neuron* **104**, 239–255.e12 (2019).
26. B. Roberts, M. C. Hendershott, J. Arakaki, K. A. Gerbin, H. Malik, A. Nelson, J. Gehring, C. Hookway, S. A. Ludmann, R. Yang, A. Haupt, T. Grancharova, V. Valencia, M. A. Fuqua, A. Tucker, S. M. Rafelski, R. N. Gunawardane, Fluorescent gene tagging of transcriptionally silent genes in hiPSCs. *Stem Cell Reports* **12**, 1145–1158 (2019).
27. M. A. Horlbeck, L. A. Gilbert, J. E. Villalta, B. Adamson, R. A. Pak, Y. Chen, A. P. Fields, C. Y. Park, J. E. Corn, M. Kampmann, J. S. Weissman, Compact and highly active next-generation libraries for CRISPR-mediated gene repression and activation. *eLife* **5**, e19760 (2016).
28. B. Laurent, L. Ruitu, J. Murn, K. Hempel, R. Ferrao, Y. Xiang, S. Liu, B. A. Garcia, H. Wu, F. Wu, H. Steen, Y. Shi, A specific LSD1/KDM1A isoform regulates neuronal differentiation through H3K9 demethylation. *Mol. Cell* **57**, 957–970 (2015).
29. W. Si, Y. Zhao, J. Zhou, Q. Zhang, Y. Zhang, The coordination between ZNF217 and LSD1 contributes to hepatocellular carcinoma progress and is negatively regulated by miR-101. *Exp. Cell Res.* **379**, 1–10 (2019).
30. S. Frietze, H. O'Geen, L. E. Littlepage, C. Simion, C. A. Sweeney, P. J. Farnham, S. R. Krig, Global analysis of ZNF217 chromatin occupancy in the breast cancer cell genome reveals an association with ERα. *BMC Genomics* **15**, 520 (2014).
31. Y. Fang, G. Liao, B. Yu, Targeting histone lysine demethylase LSD1/KDM1A as a new avenue for cancer therapy. *Curr. Top. Med. Chem.* **19**, 889–891 (2019).
32. Y. Fang, G. Liao, B. Yu, LSD1/KDM1A inhibitors in clinical trials: Advances and prospects. *J. Hematol. Oncol.* **12**, 129 (2019).
33. Y. A. T. Kasu, A. Arva, J. Johnson, C. Sajan, J. Manzano, A. Hennes, J. Haynes, C. S. Brower, BAG6 prevents the aggregation of neurodegeneration-associated fragments of TDP43. *iScience* **25**, 104273 (2022).
34. C. Proukakis, Somatic mutations in neurodegeneration: An update. *Neurobiol. Dis.* **144**, 105021 (2020).
35. D. Szklarczyk, A. L. Gable, K. C. Nastou, D. Lyon, R. Kirsch, S. Pyysalo, N. T. Doncheva, M. Legeay, T. Fang, P. Bork, L. J. Jensen, C. von Mering, The STRING database in 2021: Customizable protein–protein networks, and functional characterization of user-uploaded gene/measurement sets. *Nucleic Acids Res.* **49**, D605–D612 (2020).
36. E. Hallacli, C. Kayatekin, S. Nazeen, X. H. Wang, Z. Sheinkopf, S. Sathyakumar, S. Sarkar, X. Jiang, X. Dong, R. Di Maio, W. Wang, M. T. Keeney, D. Felsky, J. Sandoe, A. Vahdatshoar, N. D. Udeshi, D. R. Mani, S. A. Carr, S. Lindquist, P. L. De Jager, D. P. Bartel, C. L. Myers, J. T. Greenamyre, M. B. Feany, S. R. Sunyaev, C. Y. Chung, V. Khurana, The Parkinson's disease protein α-synuclein is a modulator of processing bodies and mRNA stability. *Cell* **185**, 2035–2056.e33 (2022).
37. J. Daniel, E. Liebau, The ufm1 cascade. *Cell* **3**, 627–638 (2014).
38. R. Ree, S. Varland, T. Arnesen, Spotlight on protein N-terminal acetylation. *Exp. Mol. Med.* **50**, 1–13 (2018).
39. H. Aksnes, R. Ree, T. Arnesen, Co-translational, post-translational, and non-catalytic roles of N-terminal acetyltransferases. *Mol. Cell* **73**, 1097–1114 (2019).
40. J. P. Anderson, D. E. Walker, J. M. Goldstein, R. de Laat, K. Banducci, R. J. Caccavello, R. Barbour, J. Huang, K. Kling, M. Lee, L. Diep, P. S. Keim, X. Shen, T. Chataway, M. G. Schlossmacher, P. Seubert, D. Schenk, S. Sinha, W. P. Gai, T. J. Chilcote, Phosphorylation of Ser-129 is the dominant pathological modification of α-synuclein in familial and sporadic Lewy body disease. *J. Biol. Chem.* **281**, 29739–29752 (2006).
41. R. M. de Oliveira, H. Vicente Miranda, L. Francelle, R. Pinho, É. M. Szegö, R. Martinho, F. Munari, D. F. Lázaro, S. Moniot, P. Guerreiro, L. Fonseca, Z. Marijanovic, P. Antas, E. Gerhardt, F. J. Enguita, B. Fauvet, D. Penque, T. F. Pais, Q. Tong, S. Becker, S. Kügler, H. A. Lashuel, C. Steegborn, M. Zweckstetter, T. F. Outeiro, The mechanism of sirtuin 2–mediated exacerbation of α-synuclein toxicity in models of Parkinson disease. *PLOS Biol.* **15**, e2000374 (2017).
42. M. Birol, S. P. Wojcik, A. D. Miranker, E. Rhoades, Identification of N-linked glycans as specific mediators of neuronal uptake of acetylated α-synuclein. *PLOS Biol.* **17**, e3000318 (2019).
43. A. J. Trexler, E. Rhoades, N-terminal acetylation is critical for forming α-helical oligomer of α-synuclein. *Protein Sci.* **21**, 601–605 (2012).
44. R. Bell, R. J. Thrush, M. Castellana-Cruz, M. Oeller, R. Staats, A. Nene, P. Flagmeier, C. K. Xu, S. Satapathy, C. Galvagnion, M. R. Wilson, C. M. Dobson, J. R. Kumita, M. Vendruscolo, N-terminal acetylation of α-synuclein slows down its aggregation process and alters the morphology of the resulting aggregates. *Biochemistry* **61**, 1743–1756 (2022).
45. R. Vinueza-Gavilanes, I. Íñigo-Marco, L. Larrea, M. Lasa, B. Carte, E. Santamaría, J. Fernández-Irigoyen, R. Bugallo, T. Aragón, R. Aldabe, M. Arrasate, N-terminal acetylation mutants affect α-synuclein stability, protein levels and neuronal toxicity. *Neurobiol. Dis.* **137**, 104781 (2020).
46. B. Fauvet, M.-B. Fares, F. Samuel, I. Dikiy, A. Tandon, D. Eliezer, H. A. Lashuel, Characterization of semisynthetic and naturally Nα-acetylated α-synuclein in vitro and in intact cells: Implications for aggregation and cellular properties of α-synuclein. *J. Biol. Chem.* **287**, 28243–28262 (2012).
47. A. O. Helbig, S. Rosati, P. W. W. M. Pijnappel, B. van Breukelen, M. H. T. H. Timmers, S. Mohammed, M. Slijper, A. J. R. Heck, Perturbation of the yeast N-acetyltransferase NatB induces elevation of protein phosphorylation levels. *BMC Genomics* **11**, 685 (2010).
48. U. A. Friedrich, M. Zedan, B. Hessling, K. Fenzl, L. Gillet, J. Barry, M. Knop, G. Kramer, B. Bukau, Nα-terminal acetylation of proteins by NatA and NatB serves distinct physiological roles in *Saccharomyces cerevisiae*. *Cell Rep.* **34**, 108711 (2021).
49. P. Van Damme, M. Lasa, B. Polevoda, C. Gazquez, A. Elosegui-Artola, D. S. Kim, E. De Juan-Pardo, K. Demeyer, K. Hole, E. Larrea, E. Timmerman, J. Prieto, T. Arnesen, F. Sherman, K. Gevaert, R. Aldabe, N-terminal acetylome analyses and functional insights of the N-terminal acetyltransferase NatB. *Proc. Natl. Acad. Sci. U.S.A.* **109**, 12449–12454 (2012).
50. B. van de Kooij, E. de Vries, R. W. Rooswinkel, G. M. C. Janssen, F. K. Kok, P. A. van Veelen, J. Borst, N-terminal acetylation can stabilize proteins independent of their ubiquitination. *Sci. Rep.* **13**, 5333 (2023).
51. I. Kats, A. Khmelinskii, M. Kschonsak, F. Huber, R. A. Knieß, A. Bartosik, M. Knop, Mapping degradation signals and pathways in a eukaryotic N-terminome. *Mol. Cell* **70**, 488–501.e5 (2018).
52. K. T. Nguyen, S.-H. Mun, C.-S. Lee, C.-S. Hwang, Control of protein degradation by N-terminal acetylation and the N-end rule pathway. *Exp. Mol. Med.* **50**, 1–8 (2018).
53. A. Drazic, L. M. Myklebust, R. Ree, T. Arnesen, The world of protein acetylation. *Biochim. Biophys. Acta* **1864**, 1372–1401 (2016).

54. Y. Ye, D. Klenerman, D. Finley, N-terminal ubiquitination of amyloidogenic proteins triggers removal of their oligomers by the proteasome holoenzyme. *J. Mol. Biol.* **432**, 585–596 (2020).
55. V. Vittal, L. Shi, D. M. Wenzel, K. M. Scaglione, E. D. Duncan, V. Basrur, K. S. J. Elenitoba-Johnson, D. Baker, H. L. Paulson, P. S. Brzovic, R. E. Klevit, Intrinsic disorder drives N-terminal ubiquitination by Ube2w. *Nat. Chem. Biol.* **11**, 83–89 (2015).
56. J. Zang, Y. Chen, C. Liu, L. Hu, H. Zhao, W. Ding, Y. Yuan, S. Lin, Genetic code expansion reveals aminoacylated lysine ubiquitination mediated by UBE2W. *Nat. Struct. Mol. Biol.* **30**, 62–71 (2023).
57. H.-C. Tai, E. M. Schuman, Ubiquitin, the proteasome and protein degradation in neuronal function and dysfunction. *Nat. Rev. Neurosci.* **9**, 826–838 (2008).
58. H.-J. Lee, C. Choi, S.-J. Lee, Membrane-bound α-synuclein has a high aggregation propensity and the ability to seed the aggregation of the cytosolic form. *J. Biol. Chem.* **277**, 671–678 (2002).
59. I. Dikiy, D. Eliezer, N-terminal acetylation stabilizes N-terminal helicity in lipid- and micelle-bound α-synuclein and increases its affinity for physiological membranes. *J. Biol. Chem.* **289**, 3652–3665 (2014).
60. G. Fusco, A. De Simone, P. Arosio, M. Vendruscolo, G. Veglia, C. M. Dobson, Structural ensembles of membrane-bound α-synuclein reveal the molecular determinants of synaptic vesicle affinity. *Sci. Rep.* **6**, 27125 (2016).
61. M. Lasa, L. Neri, B. Carte, C. Gázquez, T. Aragón, R. Aldabe, Maturation of NAA20 aminoterminal end is essential to assemble NatB N-terminal acetyltransferase complex. *J. Mol. Biol.* **432**, 5889–5901 (2020).
62. O. Benny, O. Fainaru, A. Adini, F. Cassiola, L. Bazinet, I. Adini, E. Pravda, Y. Nahmias, S. Koirala, G. Corfas, R. J. D'Amato, J. Folkman, An orally delivered small-molecule formulation with antiangiogenic and anticancer activity. *Nat. Biotechnol.* **26**, 799–807 (2008).
63. M. A. Carducci, D. Wang, C. Habermehl, M. Bödding, F. Rohdich, F. Lignet, K. Duecker, O. Karpenko, L. Pudelko, C. Gimmi, P. LoRusso, A first-in-human, dose-escalation study of the methionine aminopeptidase 2 inhibitor M8891 in patients with advanced solid tumors. *Cancer Res. Commun.* **3**, 1638–1647 (2023).
64. T. Heinrich, J. Seenisamy, F. Becker, B. Blume, J. Bomke, M. Dietz, U. Eckert, M. Friese-Hamim, J. Gunera, K. Hansen, B. Leuthner, D. Musil, J. Pfalzgraf, F. Rohdich, C. Siegl, D. Spuck, A. Wegener, F. T. Zenke, Identification of methionine aminopeptidase-2 (MetAP-2) inhibitor M8891: A clinical compound for the treatment of cancer. *J. Med. Chem.* **62**, 11119–11134 (2019).
65. C. R. Fields, N. Bengoa-Vergniory, R. Wade-Martins, Targeting α-synuclein as a therapy for Parkinson's disease. *Front. Mol. Neurosci.* **12**, 299 (2019).
66. R. Barbour, K. Kling, J. P. Anderson, K. Banducci, T. Cole, L. Diep, M. Fox, J. M. Goldstein, F. Soriano, P. Seubert, T. J. Chilcote, Red blood cells are the major source of α-synuclein in blood. *Neurodegener Dis* **5**, 55–59 (2008).
67. A. Caputo, Y. Liang, T. D. Raabe, A. Lo, M. Horvath, B. Zhang, H. J. Brown, A. Stieber, K. C. Luk, *Snca*-GFP knock-in mice reflect patterns of endogenous expression and pathological seeding. *eNeuro* **7**, 10.1523/ENEURO.0007-20.2020 (2020).
68. L. Neri, M. Lasa, A. Elosegui-Artola, D. D'Avola, B. Carte, C. Gazquez, S. Alve, P. Roca-Cusachs, M. Iñarrairaegui, J. Herrero, J. Prieto, B. Sangro, R. Aldabe, NatB-mediated protein N-α-terminal acetylation is a potential therapeutic target in hepatocellular carcinoma. *Oncotarget* **8**, 40967–40981 (2017).
69. S. Deng, B. Pan, L. Gottlieb, E. J. Petersson, R. Marmorstein, Molecular basis for N-terminal α-synuclein acetylation by human NatB. *eLife* **9**, e57491 (2020).
70. F. A. Ran, P. D. Hsu, J. Wright, V. Agarwala, D. A. Scott, F. Zhang, Genome engineering using the CRISPR-Cas9 system. *Nat. Protoc.* **8**, 2281–2308 (2013).
71. M. D. Leonetti, S. Sekine, D. Kamiyama, J. S. Weissman, B. Huang, A scalable strategy for high-throughput GFP tagging of endogenous human proteins. *Proc. Natl. Acad. Sci. U.S.A.* **113**, E3501–E3508 (2016).
72. A. Sasaki, S. Arawaka, H. Sato, T. Kato, Sensitive Western blotting for detection of endogenous Ser^{129}-phosphorylated α-synuclein in intracellular and extracellular spaces. *Sci. Rep.* **5**, 14211 (2015).
73. N. N. Naseri, B. Ergel, P. Kharel, Y. Na, Q. Huang, R. Huang, N. Dolzhanskaya, J. Burré, M. T. Velinov, M. Sharma, Aggregation of mutant cysteine string protein-α via Fe-S cluster binding is mitigated by iron chelators. *Nat. Struct. Mol. Biol.* **27**, 192–201 (2020).
74. H. Wickham, M. Averick, J. Bryan, W. Chang, L. McGowan, R. François, G. Grolemund, A. Hayes, L. Henry, J. Hester, M. Kuhn, T. Pedersen, E. Miller, S. Bache, K. Müller, J. Ooms, D. Robinson, D. Seidel, V. Spinu, K. Takahashi, D. Vaughan, C. Wilke, K. Woo, H. Yutani, Welcome to the tidyverse. *J. Open Source Softw.* **4**, 1686 (2019).
75. Y. Perez-Riverol, J. Bai, C. Bandla, D. García-Seisdedos, S. Hewapathirana, S. Kamatchinathan, D. J. Kundu, A. Prakash, A. Frericks-Zipper, M. Eisenacher, M. Walzer, S. Wang, A. Brazma, J. A. Vizcaíno, The PRIDE database resources in 2022: A hub for mass spectrometry-based proteomics evidences. *Nucleic Acids Res.* **50**, D543–D552 (2022).
76. C. Y. Chung, V. Khurana, P. K. Auluck, D. F. Tardiff, J. R. Mazzulli, F. Soldner, V. Baru, Y. Lou, Y. Freyzon, S. Cho, A. E. Mungenast, J. Muffat, M. Mitalipova, M. D. Pluth, N. T. Jui, B. Schüle, S. J. Lippard, L.-H. Tsai, D. Krainc, S. L. Buchwald, R. Jaenisch, S. Lindquist, Identification and rescue of α-synuclein toxicity in Parkinson patient-derived neurons. *Science* **342**, 983–987 (2013).
77. X. Yang, V. Malik, R. Jauch, Reprogramming cells with synthetic proteins. *Asian J. Androl.* **17**, 394–402 (2015).
78. S. Tyanova, T. Temu, J. Cox, The MaxQuant computational platform for mass spectrometry-based shotgun proteomics. *Nat. Protoc.* **11**, 2301–2319 (2016).
79. C. Bielow, G. Mastrobuoni, S. Kempa, Proteomics quality control: Quality control software for MaxQuant results. *J. Proteome Res.* **15**, 777–787 (2016).

Acknowledgments: We would like to thank members of the Shalem laboratory for discussions and M. Ward from NIH for sharing the i3 iPSC line. We thank E. Lee for the critical review of the manuscript. We thank C. W. Ross III (Director: Automated Synthesis and Characterization of Penn Chemistry) and R. Kubanoff (BCRC Lab Manager) for providing the Bruker rapifleX MALDI Tof-Tof (NIH grant no. 1S10OD030460-01). We also thank A. Caputo from K.L.'s laboratory and K.A. from E.R's laboratory for the experimental work that was not included in the final version of the manuscript. **Funding:** This work was supported by two grants from the Michael J. Fox Foundation 15556 awarded to O.S. and K.L. and 23435 awarded to O.S. and E.R. and from a pilot Transdisciplinary Awards Program in Translational Medicine and Therapeutics (TAPITMAT) from the University of Pennsylvania awarded to O.S. and K.L. Additional funding support was provided by the following NIH grants: DP2GM137416 and R03NS111447 to O.S., R01NS088322 and AG62418 to K.L., R01NS120625 to E.R., R01NS109209 and 1R01NS128142-01A1 to V.K., F32-AG079537 to N.N.N., and T32GM132039 to K.A. Additional support includes a CURE grant (SAP #4100083086) from the Pennsylvania Department of Health to O.S. and Aligning Science Across Parkinson's Disease (ASAP-000472) to V.K. V.K. was also supported as an NYSCF Stem Cell Robertson Investigator (NYSCF-R-I49) and George C. Cotzias Fellow of the American Parkinson's Disease Association. **Author contributions:** Conceived and designed the project: O.S., K.L., and S.S.K. Conducted experiments and acquired data: S.S.K. led this study and performed all the experiments described in the manuscript excluding some as mentioned: Figs. 1H and 4D were performed by C.B. The data for Fig. 4F were produced by J.R., H.F., and L.A.S. (members of the CHOP/UPenn proteomics core). N.N.N. directed and performed the mechanism experiments and generated data for the following: Figs. 3G, 5 (A to C), and 7 and figs. S5 (A to D, F, and G) and fig. S7. E.H. and A.N. generated the SNCA Triplication iPSCs and the copy number–corrected control iPSC lines. S.R.P. assisted with the secondary neuronal screen. Supervision: E.R. oversaw work provided by N.N.N. and K.A. V.K. oversaw iPSC generation by E.H. and A.N.. Data analysis: O.S. and S.S.K. Writing—original draft: O.S. and S.S.K. Writing—review and editing: N.N.N., K.L., and E.R. All authors read and approved the final manuscript. **Competing interests:** The authors declare that they have no competing interests. **Data and materials availability:** All data needed to evaluate the conclusions in the paper are present in the paper and/or the Supplementary Materials. The MS proteomics data have been deposited to the ProteomeXchange Consortium via the PRIDE (*75*) partner repository with the dataset identifier PXD048283.

Submitted 2 July 2023
Accepted 11 January 2024
Published 9 February 2024
10.1126/sciadv.adj4767